Thomas Puffitsch, BSc

Modeling the Fluidization Behavior of Polydisperse Fine Powders in a Segregation Tester

MASTER'S THESIS

to achieve the university degree of

Diplom-Ingenieur

Master's degree program: Chemical and Process Engineering

submitted to

Graz University of Technology

Supervisor

Ass.Prof. Dipl.-Ing. Dr.techn. Stefan Radl

Institute of Process and Particle Engineering

Graz, May 2016

EIDESSTATTLICHE ERKLÄRUNG

Ich erkläre an Eides statt, dass ich die vorliegende Arbeit selbstständig verfasst, andere als die angegebenen Quellen/Hilfsmittel nicht benutzt, und die den benutzten Quellen wörtlich und inhaltlich entnommenen Stellen als solche kenntlich gemacht habe. Das in TUGRAZonline hochgeladene Textdokument ist mit der vorliegenden Masterarbeit identisch.

AFFIDAVIT

I declare that I have authored this thesis independently, that I have not used other than the declared sources/resources, and that I have explicitly indicated all material which has been quoted either literally or by content from the sources used. The text document uploaded to TUGRAZonline is identical to the present master‘s thesis.

6.5. 2016

Date

T. [illegible], BSc

Signature

Abstract

In the pharmaceutical industry size or density based segregation of dry powders can be critical with respect to product quality. To be able to determine the segregation tendency of a powder (or a powder blend) in a certain industrial application, computer simulations have become more and more important. Thus, the development of accurate numerical models is essential for the reliable prediction of the segregation tendency of a given particulate system.

First, we investigate the rheology of dense polydisperse cohesive granular matter using the Discrete Element Method (DEM). While the rheology of the cohesive powder can be studied in the widely used shear setup utilizing Lees-Edwards boundary conditions [J Phys. C: Solid State Phys. 5 (1972), 1921-1929], this setup fails in predicting the macroscopic cohesion of the powder. Thus, a new shear setup is proposed and applied to calibrate the cohesion parameters in the DEM using experimentally determined yield loci.

Second, it is shown that the scaling of the cohesion model, based on a granular Bond number, yields accurate predictions in a dense flow regime. Specifically, we show that a van der Waals cohesion model, in case it is correctly scaled, can be used to perform scaled DEM-based (i.e. parcel-based) simulations of cohesive polydisperse powders.

Third, we have performed CFD-DPM simulations of a polydisperse powder with up to 3 Mio. particles, and a maximum size ratio of ten. The results show that the formulation of the drag force has – besides cohesion – a huge influence on the flow pattern, and thus also on the segregation behavior. While a simple drag model for monodisperse flows indicates a marked tendency for segregation, an advanced drag formulation for polydisperse flows fails to predict segregation. Finally, we find a certain influence of the computational grid on the simulation results. This leads us to the conclusion that grid-size effects should be carefully investigated in follow-up studies.

Kurzfassung

In der pharmazeutischen Industrie können Größen- und Dichteunterschiede zur Segregation von pulverförmigen Medien und damit zu Problemen bei der Produktqualität führen. Um die Segregationstendenz eines Pulvers (oder einer Pulvermischung) bei der Verarbeitung bestimmen zu können, werden in den letzten Jahren vermehrt Computersimulationen eingesetzt. Darum ist die Entwicklung von akkuraten numerischen Modellen essenziell für die zuverlässige Vorhersage der Segregationseigenschaften eines vorhandenen Pulvers.

Zu Beginn untersuchen wir die Rheologie von dichten polydispersen kohäsiven Pulvern mit Hilfe der Diskreten Elemente Methode (DEM). Während die Rheologie von kohäsiven Pulvern in einer einfachen Scherströmung mit Lees-Edwards Randbedingungen [J Phys. C: Solid State Phys. 5 (1972), 1921-1929] untersucht werden kann, versagt dieses Setup bei der Vorhersage der makroskopischen Kohäsion des Pulvers. Darum wird hier ein neues Setup vorgeschlagen und verwendet, welches die Kalibrierung der Kohäsionsparameter in der DEM anhand experimentell gemessener Fließorte zulässt.

Des Weiteren wird gezeigt, dass die Skalierung des Kohäsionsmodells, basierend auf einer granularen Bondzahl, zu exakten Vorhersagen im dichten Strömungsregime führt. Es wird gezeigt, dass mit einem Van der Waals Kohäsionsmodell, sofern es richtig skaliert ist, das Fließverhalten von kohäsiven Pulvern in einer skalierten DEM korrekt vorhergesagt werden kann.

Weiters werden CFD-DPM Simulationen von kohäsiven Pulvern mit bis zu 3 Mio. Partikeln und einem maximalen Größenverhältnis von 1:10 durchgeführt. Die Ergebnisse zeigen, dass das verwendete Widerstandskraft-Modell – neben der Kohäsion – großen Einfluss auf die Strömung und damit auf das Segregationsverhalten hat. Während Simulationen mit einem einfachen Widerstandskraft-Modell für monodisperse Fluid-Partikelsysteme Segregation vorhersagen, versagt ein weiterentwickeltes Modell für polydisperse Strömungen bei der Prognose von Segregation. Außerdem wird der Einfluss des Rechengitters untersucht. Diese Studien zeigen einen Einfluss der Gitterauflösung auf die Ergebnisse, weshalb diese Effekte bei weiteren Studien beachtet werden sollten.

Acknowledgement

I would like to express my deepest gratitude to my supervisor, Ass.Prof. Stefan Radl, for the continuous support and guidance during the making of my master thesis. His patience, rigor and bright ideas were crucial for this work.

I am grateful to the DCS computing GmbH for their cooperation, and for providing financial support to complete this thesis.

I would like to acknowledge the use of HPC resources provided by the ZID of Graz University of Technology.

I am also indebted to my friends and colleagues at the TU Graz, who supported me throughout the writing this thesis, in particular Christoph Fuchs, who always helped me with words and deeds during my whole study.

Last but not least, I would like to thank my family for their unconditional support during my Chemical and Process Engineering study years. Especially, I want to thank my partner Ines, who always supported me for the last, crucial period.

Table of Content

List of Figures

List of Tables

Abbreviations

API	Active pharmaceutical ingredient
BC	Boundary conditions
CFD	Computational fluid dynamics
CFDEM®	Open-source software for coupling of CFD and DEM
DEM	Discrete element method
DMT	Derjaduin-Muller-Toporov
DPM	Discrete parcel method
EPSD	Elastic-plastic spring-dashpot model
JKR	Johnson-Kendall-Roberts
LIGGGHTS®	LAMMPS Improved for General Granular and Granular Heat Transfer Simulations
OpenFOAM®	Open-source field operation and manipulation software
PSD	Particle size distribution

Nomenclature

Latin Symbols

A	cross sectional area	m^2
Bo	gravity-based Bond number	-
Bo^*	stiffness-based Bond number	-
CG	coarse graining ratio	-
d	diameter	m
$\mathbf{F}$	force	N
$\mathbf{g}$	gravity	$\mathrm{m\ s}^{-2}$
h	height	m
Ha	Hamaker constant	N m
I	rotational moment of inertia	$\mathrm{kg\ m}^2$
k	spring stiffness	$\mathrm{N\ m}^{-1}$
l	length	m
$\mathbf{l}^{pc}$	distance between particle center and contact	m
m	mass	kg
N	number	-
p	pressure	Pa
ΔQ_0	number fraction of particles in a certain class	-
ΔQ_3	volume fraction of particles in a certain class	-
r	particle radius	m
r_{ij}	mean radius of particles i and j	m
Re	Reynolds number	-
s	surface-to-surface distance between two particles	m
t	time	s
Δt	simulation timestep	s

$\mathbf{T}$	torque	N m
$\mathbf{u}_f$	average fluid velocity	m s^{-1}
$\mathbf{U}_{mf}$	minimum (superficial) fluidization velocity	m s^{-1}
$\mathbf{u}_p$	average particle velocity	m s^{-1}
$\mathbf{u}'_p$	particle velocity fluctuation	m s^{-1}
$\mathbf{U}_0$	superficial fluid velocity	m s^{-1}
V	volume	m^3
v_{char}	characteristic velocity	m s^{-1}
w_p	particle weight	kg
$\mathbf{x}$	particle position	m
Y	Young’s modulus	Pa

Greek Symbols

δ	particle overlap	m
ε	coefficient of restitution	-
$\dot{\gamma}$	shear rate	s^{-1}
μ	coefficient of friction	-
ν	kinematic viscosity	m^2 s^{-1}
ν_p	Poisson ratio	-
ρ	density	kg m^{-3}
$\boldsymbol{\sigma}$	stress tensor	Pa
σ	pressure (or hydrostatic stress)	Pa
σ_{ii}	normal component of the stress tensor	Pa
$\boldsymbol{\tau}$	deviatoric stress tensor	Pa
τ_{ij}	shear component of the stress tensor	Pa

ϕ	particle volume fraction	-
$\boldsymbol{\omega}$	angular velocity	rad s^{-1}

Sub- and Superscripts

bed	particle bed
bin	bin
box	simulation box
c	contact
d	drag
cell	cell
coh	cohesion
cons	consolidation
cont	contact
f	fluid
final	final
g	gravity
high	upper limit
in	inner section
kin	kinetic
low	lower limit
max	maximum
min	minimum
n	normal
out	outer section
p	particle
ref	reference

shear	shear
t	tangential
vdW	van der Waals
x, *y*, *z*	position in Cartesian space
32	Sauter mean (diameter)
^	dimensionless value
‒	arithmetic mean value

1 Introduction

Granular materials are used in a wide field of applications in industry, such as combustion plants (e.g. coal, biomass), pharmaceutical industry (e.g. API, excipients), and chemical industry. Granular materials often consist of particles of different sizes, shapes, and material properties. The particle size distributions (PSDs) of such materials normally span a few orders of magnitude, which can be a source of challenges during the processing, the handling, or the storage of the materials due to demixing effects, i.e. segregation [1]. Therefore, a large number of research activities focused on the main influencing factors for segregation, namely difference in the particle size, and/or in particle density [2–6]. Also, cohesion plays an important role, because small particles can stick together, and hence cohesion can effectively suppress segregation [7].

In the pharmaceutical industry, fluidization of dry powders or granules often causes segregation, consequently negatively influencing the product quality [7]. Thus, experimental devices were developed in the past to quantify the segregation tendency of a powder, or a powder blend [3,7–10]. The main disadvantages of these experimental investigations are that (i) a limited amount of the materials to be tested is available during product development, (ii) issues with the reproducibility of the tests, and (iii) the rather limited information gained from the experiments (i.e. typically only integral quantities can be experimentally measured). Moreover, the exposure of the operators to hazardous materials is a severe safety risk [7], often critically limiting access to experimental data, or resulting in high costs.

Numerical simulations typically allow a more detailed investigation of particulate systems, however, are often limited by restrictions imposed by the underlying physical models. Fortunately, the development of realistic physical models has significantly accelerated within the last decades, so that nowadays often results of numerical simulations are more accurate than data extracted from physical experiments. For example, nowadays the rheology of dense particulate systems is typically probed with numerical simulations only, and such studies have been published with increasing frequency in the past fifteen years [11–17]. In the same period of time, the segregation tendency in fluidized beds using DEM and CFD-DEM simulations was investigated [18–20], again highlighting the importance of numerical work in the field. These advances in the field of numerical tools and models also motivate the present work, which is solely dedicated to DEM, CFD-DEM and CFD-DPM simulations of cohesive polydisperse granular matter. Notwithstanding this fact, it is clear that in order to describe these complex granular systems, reference experiments are inevitable to identify critical system parameters. Unfortunately, critical system parameters (e.g. to characterize cohesive particle-particle interactions) cannot be simply measured in an experiment, due to the delicate interactions of particle morphology, cohesion and segregation tendency. Thus, a fruitful strategy is the calibration of models by means of a tight integration of experimental data with computer simulations. Exactly such a calibration workflow is the ultimate goal of the present study.

1.1 Goals

This thesis focuses on the establishment of a workflow for the simulation of segregation profiles in a lab-scale segregation tester (i.e. the one presented by Hedden et al. [7]). Specifically, the segregation behavior of a polydisperse cohesive powder bed shall be investigated using a CFD-DPM approach [21,22]. The main tasks of this work are as follows:

- review of cohesion force models for DEM simulations of dry powders and their possibility to be used in coarse-grained, i.e. parcel-based, simulations.
- investigation of the rheology of polydisperse cohesive powders.
- investigation of the influence of cohesion on the yield locus in a shear flow.
- investigation of the segregation tendency of polydisperse cohesive powders in scaled CFD-DPM simulations.
- a workflow for scaled simulations in a lab-scale segregation tester.

2 State of the Art

2.1 DEM Basics

The discrete element method (DEM) tracks individual particles and calculates their translational and rotational motion. It is a so called Lagrangian model, in contrast to Eulerian (continuum) models that predict particle motion on a fixed computational grid. Specifically, DEM solves Newton's equation of motion for force and momentum, which read [23]:

$$\frac{d\left(m_p \mathbf{v}\right)}{dt} = \sum \mathbf{F} \tag{2.1}$$

$$\frac{d\left(I_p \boldsymbol{\omega}\right)}{dt} = \sum \mathbf{T} \tag{2.2}$$

In other words, all relevant forces and torques acting on each particle are summed up, and integrated (the position and orientation of the particles can then be determined in a straight forward manner). Depending on the purpose of the simulation, these forces are (i) contact forces, (ii) volumetric forces (e.g. gravitational forces), (iii) cohesion forces, or (iv) hydrodynamic (e.g. drag) forces originating from a surrounding fluid.

In general, particles in simulations using the DEM can be modeled as perfectly rigid (i.e. the so-called hard-sphere approach), or as slightly elastic (i.e. soft-sphere approach). The hard-sphere approach is based on instantaneous collisions of rigid spheres, and thus limited to dilute or moderately dense systems [1]. The soft-sphere approach models particle collisions with an elastic-plastic spring-dashpot model (EPSD), which allows the particles to overlap [24]. Various types of EPSD models exist, the simplest one being the linear (or "Hookean") EPSD, in which the spring stiffness k is constant. Thus, the normal force acting on colliding particles is linearly proportional to their overlap δ. In contrast, the (more realistic) Hertzian EPSD model models the spring stiffness to be proportional to $\sqrt{\delta}$, and hence the contact force is proportional to $\sqrt{\delta^3}$ [25]. The tangential force between two colliding particles is limited by the Coulomb criterion $\left|\mathbf{F}_t\right| \le \mu \left|\mathbf{F}_n\right|$ [25]. Note that, for the calculation of the tangential force, the cohesion force must not be accounted for when computing $\mathbf{F}_n$ in this expression. Instead, the tangential force must be calculated based on the normal contact force only.

2.1.1 The Parcel Approach

Due to limited computational resources, the maximum number of particles, as well as the maximum size ratio (defined as the largest to smallest particle size) in DEM simulations is constrained. This makes the simulation of large-scale units with a straight forward application of the DEM infeasible. To overcome this obstacle, the discrete parcel method (DPM) was introduced [21,22,26].

For instance, Bierwisch et al. [21] proposed a parcel based model for the Hertzian contact model, where the diameter of the particles is artificially enlarged, or “coarse-grained”. Similarly, such a coarse graining can be performed for the Hookean EPSD model [22]. Using this approach, the number of particles can be significantly reduced, and the simulation time step can be increased. In the Hertzian model the particle density, the Young’s modulus, the coefficient of restitution, and the coefficient of friction are scale invariant. For the Hookean model, the spring stiffness divided by the particle diameter has to be scale invariant. Unfortunately, such a coarse graining idea yields scale-invariant stresses only in the quasi-static regime, and over-predicts stresses in the inertial regime as shown by Radl et al. [22]. This over-prediction is often acceptable, since stresses in the inertial regime are, anyhow, orders of magnitude lower compared to that in the quasi-static regime.

2.2 The CFD-DEM Approach

One possibility to numerically calculate the movement of particles in a surrounding fluid is the CFD-DEM approach: Here, the fluid motion is calculated with a computational fluid dynamics (CFD) software, and coupled with the particle motion solver (typically based on the DEM) via phase-coupling models. CFDEM® is a powerful tool to perform these simulations. It combines the open-source software package OpenFOAM® (for simulating the fluid motion) with the granular dynamics software LIGGGHTS®. Most important, CFDEM® realizes a so-called two-way coupling between the particle and fluid phase, i.e. particles experience the presence of the fluid and vice versa. Thus, Newton’s third law of motion (action-reaction) can be ensured, allowing the consistent simulation of (theoretically) arbitrarily dense suspension flows.

Unfortunately, the direct numerical simulation of the fluid flow through the interstices of the particle bed would be computationally too expensive. As a compromise, the CFD grid size is set larger than the particle diameter. This results in a need for additional models for the forces exerted by the fluid on the particles: essentially, (i) models accounting for unresolved fluctuations of pressure and fluid velocity near the surface of the particle, as well as (ii) models that account for an average fluid stress field need to be considered. Typically, the drag force, and the buoyancy force are modeled, and some more delicate effects (e.g. the Basset history force, or effects due to the deviatoric fluid stress) are neglected. In this work, the drag model of Beetstra et al. [27] for monodisperse dense flows, as well as the model of Holloway et al. [28] - which is based on Beetstra et al. [27] - for polydisperse dense flows are used. While we focus on models for cohesive forces in the next chapter, a detailed description of these two drags models can be found in Appendix A.1.

3 Theoretical Model

We next focus on some details of our theoretical model used to simulate the flow of cohesive polydisperse powder beds. When dealing with powders (i.e. granular matter involving particles with a size of typically less than 1 mm), gravity may not be the dominant force any more. Instead, inter-particle forces – such as van der Waals or electrostatic forces – are significant, and hence must be considered. As a rule of thumb, van der Waals forces have to be considered for particle sizes less than 100 µm [29,30], depending on the particle's surface roughness. Electrostatic forces are of considerable magnitude even for larger particles, and are characterized by a comparably long-range potential. Furthermore, electrostatic forces depend on the particle charge, which is difficult to predict. Consequently, conclusive numerical studies dedicated to the effects of electrostatic forces on particle flow are virtually absent in literature. Hence, we have decided to leave out this delicate topic in line with the opinion present in the literature. Thus, we purely focus on van der Walls type cohesive interactions between particles for the time being.

The van der Waals force – in a broader sense – includes the dipole/dipole, the dipole/non-polar, and the non-polar/non-polar (so called dispersion, or London) forces between molecules, and macroscopic bodies. Hamaker [31] analyzed the London van der Waals forces between spherical particles as a result of fluctuating dipoles on an atomic level. While inter-molecular forces decay with the separation distance s as s^{-7}, the attractive force between macroscopic bodies decreases only with s^{-2} [30]. Different to other inter-molecular, or inter-particle forces, vdW forces are omnipresent, and can only be influenced by (i) the interstitial fluid or (ii) the surface roughness of the particles [32].

In the context of a numerical modeling, significant effort has been devoted to find accurate, yet computationally efficient expressions to predict van der Waals cohesion forces. Specifically, two basic types of models are frequently used in the literature:

- The Hamaker model [30] – or further called van der Waals model – calculates the attractive force, based on an interaction constant, i.e. the Hamaker constant, and on the particles' surface distance. Most important, this model was modified by Ye et al. [33], and this modification is also used in the current work. Rumpf [34] first proposed a Hamaker model which takes into account the asperity of the particle surfaces. This model was further modified and extended by different groups (e.g. [35,36]). Since, in this work, the roughness of the particles is not further investigated, these models are not accounted for here. More recently, Gu et al. [37] proposed a modified Hamaker model to take the particle stiffness into account, which is, however, not further considered here either.

- The JKR [38], and the DMT [39] model calculate the force between deformable smooth particles, based on their overlap. Unfortunately, for parcel-based models, recent research indicates inconsistent results when performing shear test simulations involving the JKR model [40,41]. Hence, we have decided not to pursue the idea of a JKR model in the present work.

3.1 The van Der Waals Cohesion Model

The van der Waals cohesion force model acts – contrary to most of the other cohesion models – even in case particles are not in contact. This needs a more complex implementation of the vdW cohesion model, compared to other cohesion models, in which the attractive force is only accounted for in case of contact (e.g. the simplified JKR models available in LIGGGHTS®). In the current work, the vdW model proposed by Ye et al. [33] is used, which calculates the magnitude of the attractive force between two particles as follows:

$$\left|\mathbf{F}_{vdW}\left(s\right)\right| = \frac{Ha}{3} \cdot \frac{2 r_i r_j \left(r_i + r_j + s\right)}{\left(s\left(2 r_i + 2 r_j + s\right)\right)^2} \cdot \left[\frac{s\left(2 r_i + 2 r_j + s\right)}{\left(r_i + r_j + s\right)^2 - \left(r_i - r_j\right)^2} - 1\right]^2 \tag{3.1}$$

Here *Ha* is the Hamaker constant, r_i and r_j are the radii of particles *i* and *j*, respectively, and *s* is the particle-particle surface distance. In this model the cohesion force does diverge to infinity at particle contact. Thus, a minimum cutoff distance s_{min} has to be defined. Two different definitions for this distance can be found in literature: (i) a constant cutoff distance, and (ii) a particle size dependent cutoff distance. In literature, a constant surface distance between 0.3 and 1 nm is widely used [33,35,42,43]. This lies within the range of the inter-molecular distance of about 0.4 nm whenever the surfaces of the particles are “touching” each other [44]. The latter, i.e. a particle size dependent cutoff, was applied by some authors for monodisperse systems [11,14]. In polydisperse systems, however, the van der Waals force would increase with decreasing particle size, and thus model a lower asperity for smaller particles. Consequently, in the current work a constant minimum cutoff distance of 0.4 nm is used. For smaller distances (or overlap of the particles) the vdW force is constant and taken to be the value at the cutoff distance.

Out of numerical reasons, it is not efficient to compute particle-particle interaction forces for large surface separation distances. Hence, a cut-off distance is typically imposed to speed up the simulations. Fortunately, the vdW force decreases rapidly with the separation distance, so that a maximum cutoff distance of $s_{max} = 0.25 d_p$ is widely used in literature [11,14,42]. Particle interactions beyond this limit are negligible. For the polydisperse particles used in this work the maximum cutoff distance is defined as follows:

$$s_{max} = 0.25\left(r_i + r_j\right) \tag{3.2}$$

In the limit of small *s* (i.e. in case *s* is much smaller than one of the particle radii, $s << r_i, r_j$) expression (3.1) is reduced to the simpler Hamaker model [42]:

$$\left|\mathbf{F}_{vdW}\left(s\right)\right| = \frac{Ha}{12}\frac{r_{ij}}{s^2}\,, \tag{3.3}$$

with

$$r_{ij} = \frac{2 r_i r_j}{r_i + r_j}\,. \tag{3.4}$$

In Fig. 1 the scaled magnitude of the force between two particles for both the full and the simple van der Waals cohesion models are compared for large separation distances. The particle radii are 10^{-3} m and 10^{-4} m, respectively. The maximum surface distance as defined in Eqn. (3.2) was used for the calculations. One can see that – in this case – the simplified and the full van der Waals model differ only for relative surface distances larger than 10^{-2}. The relative difference between the two models at the maximum cutoff distance is:

$$\frac{\left|\mathbf{F}_{vdW}^{simple}(s_{max})\right| - \left|\mathbf{F}_{vdW}^{full}(s_{max})\right|}{\left|\mathbf{F}_{vdW}^{full}(s_{max})\right|} = 639\% \tag{3.5}$$

This difference seems large, but compared to the maximum cohesion force between the particles (i.e. the force a $s_{min} = 0.4nm$), the force is very small at the cutoff distance:

$$\frac{\left|\mathbf{F}_{vdW}^{full}(s_{max})\right|}{\left|\mathbf{F}_{vdW}^{full}(s_{min})\right|} = 2.8 \cdot 10^{-13} \tag{3.6}$$

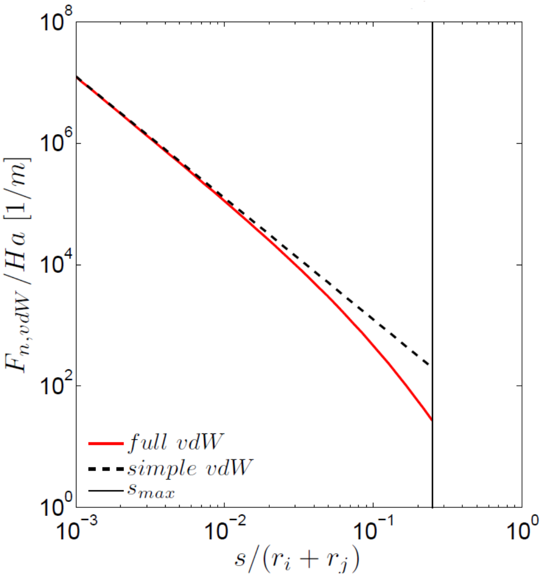

Fig. 1: Comparison of the force between two particles for the full and the simple van der Waals cohesion model with particle radii 10^{-3} m and 10^{-4} m, respectively.

3.1.1 The Bond Number

The influence of inter-particle cohesion on particle motion can be quantified via the dimensionless van der Waals force, specifically, the cohesive granular Bond number [42]. The gravity-based (and classically used) Bond number is defined as the maximum cohesion force, compared to the magnitude of the gravitational force acting on a particle [16]:

$$Bo = \frac{\left|\mathbf{F}_{coh}^{max}\right|}{\left|\mathbf{F}_{g}\right|} \tag{3.7}$$

In case gravity has only a minor effect on a simulation (e.g. in very dense regions), or is not even accounted for in a simulation, an alternative definition must be used. For example, Gu et al. introduced a modified Bond number, based on a characteristic contact force [14]. Depending on the contact model used in the simulation, this “stiffness-based” Bond number has different definitions, which read as follows:

For the Hookean contact model:

$$Bo^* = \frac{\left|\mathbf{F}_{coh}^{max}\right|}{k_n\, d_p}, \tag{3.8}$$

and for the Hertzian contact model:

$$Bo^* = \frac{\left|\mathbf{F}_{coh}^{max}\right|}{Y\, d_p^2} \, . \tag{3.9}$$

It must be stressed that these two alternative definitions of the Bond number have a fundamentally different meaning: While the gravity-based Bond number quantifies the "stickiness" in a gravitationally-driven flow, the stiffness-based Bond number has the meaning of a dimensionless overlap between contacting (cohesive) particles.

3.1.2 Scaling of the Cohesion Model in Coarse-Grained Simulations

When performing DPM simulations, the van der Waals cohesion model can be scaled based on the Bond numbers defined in the previous section. The gravity-based Bond number scales according to:

$$Bo = \frac{Ha}{d_p^2} \frac{1}{4\pi\, \rho_p \left|\mathbf{g}\right| s_{min}^2} \tag{3.10}$$

The second part of this equation is not affected by coarse graining, and hence remains constant upon scaling the particle diameter. Thus, the gravity-based scaling of the Hamaker constant must follow:

$$Ha \propto CG^2 \tag{3.11}$$

The stiffness-based Bond numbers for Hookean and Hertzian contact model leads to:

$$Bo^* = \frac{Ha}{k_n} \frac{1}{24 s_{min}^2} \, , \tag{3.12}$$

and

$$Bo^* = \frac{Ha}{d_p} \frac{1}{24 Y s_{min}^2} \, , \tag{3.13}$$

respectively. Here the spring constant scales linearly with the coarse graining ratio [22]. In both cases, the stiffness-based scaling for parcel-based simulations is:

$$Ha \propto CG \, , \tag{3.14}$$

and hence is independent of the EPSD model used. It has to be mentioned, that these scaling rules are only valid in case a constant minimum surface distance is applied (see section 3.1).

For the polydisperse granular materials considered in the present work, an appropriate reference particle size must be used. Specifically, we have based the Bond number on the Sauter mean diameter:

$$d_{32} = \frac{\sum_i^{N_p} d_i^3}{\sum_i^{N_p} d_i^2} \tag{3.15}$$

The reference value for the normal spring stiffness k_n, used in the Hookean contact model, was also calculated with d_{32} in order to be consistent.

4 Shear Box Simulations

The goals of the shear box simulations are (i) to investigate the granular rheology of the polydisperse cohesive powder used in this work, and (ii) to find a quick and easy way to quantify the effect of cohesion parameters on the powder's rheology. These simulations should be then used to calibrate the Hamaker constant based on the experimentally determined yield locus (i.e. the macroscopic cohesion) of the powder.

Schwedes [45] reviewed the most common experimental devices to measure flow properties of bulk solids. Specifically, these are (i) the Jenike shear cell [46], (ii) various torsional shear cells (e.g. annular shear cells, with the most prominent example being the Schulze ring shear tester defined in ASTM D6773), or (iii) uniaxial testers (e.g. [47]). In addition, the widely used Freeman FT4 powder rheometer (Freeman Technology, Malvern, UK) has to be mentioned here, which belongs to the group of torsional cells. Many researchers also use those devices as a starting point for their numerical studies, e.g. Luding and Alonso-Marroquín [48], or Singh et al. [16]. For example, Schwarze et al. [12] investigated the effect of cohesion (due to liquid bridges) on powder properties in a split bottom annular shear cell. Yan et al. [41] numerically investigated powder flowability of cohesive powders in an FT4 rheometer.

Nevertheless, the simulation of real experimental devices implies some disadvantages: (i) the influence of wall effects on the monitored variables, and (ii) the simulations are often limited to monodisperse systems, due to the size of the devices and the limited number of particles that can be used in simulations. Thus, this section focuses on the simulation of small – but representative – unbounded powder samples.

4.1 *Shear Setup with Lees-Edwards BC*

In a first step the granular rheology of the polydisperse powder is investigated by homogeneously shearing a sample in a three-dimensional periodic setup. This is realized by applying the widely used Lees-Edwards boundary conditions [49]. Our setup matches that of Gu et al. [14]. The chosen simulation parameters are documented in the following.

4.1.1 Simulation Setup

The simulations are performed for different mean particle volume fractions in the domain. Thus, in a first step the number of particles has to be calculated, based on the PSD and the size of the (cubic) shear box. After randomly inserting the predefined number of particles in a somewhat larger domain, the domain is uniaxially compacted in shear direction, i.e. in *x*-direction, to reach a homogeneous, more or less densely packed particle sample.

Subsequently, the particle sample is continuously sheared until the stresses reach constant values. To achieve this, a constant dimensionless shear rate is defined as follows:

$$\hat{\dot{\gamma}} = \frac{\dot{\gamma}\, d_{32}}{\sqrt{k_{n32} / (\rho_p\, d_{32})}} \tag{4.1}$$

The principle of the shear flow involving Lees-Edwards boundary conditions can be seen in Fig. 2. The applied shear results in a linear velocity profile in the shear gradient direction, i.e. in the *y*-direction.

Once the monitored normal stress and the shear stress in *xy*-direction (see Appendix A.2 for more information) have approached a statistical steady state, the simulations can be stopped, and the mean stresses are calculated by time averaging.

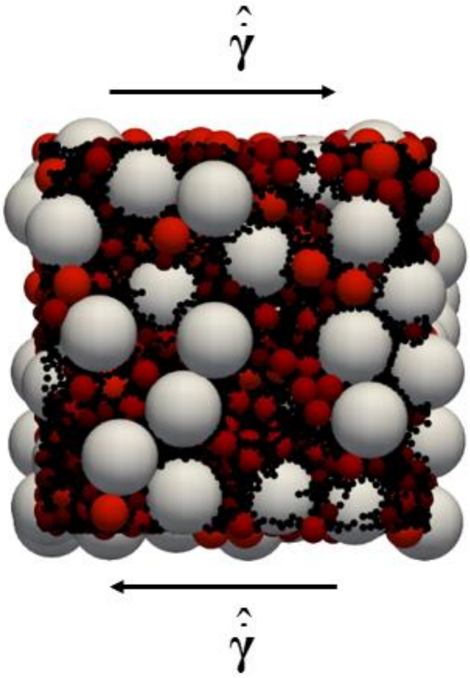

Fig. 2: Setup of the shear tests that apply Lees-Edwards boundary conditions.

4.1.2 Simulation Parameters

In this work, assemblies of spherical particles with a uniform (volume-based) particle size distribution[1] (PSD) are investigated. The shear tests with Lees-Edwards BC are performed with particle diameters between 5 – 1000µm. The continuous PSD is divided into five classes with mean particle diameters ranging from 70 – 700µm. Thus, a maximum size ratio of 10 is used to save computation time. The volume fraction of each class *i* for the uniform PSD is calculated with:

$$\Delta Q_{3,i} = \frac{d_{p,high,i} - d_{p,low.i}}{d_{p,high,5} - d_{p,low,1}} \tag{4.2}$$

Consequently, the number fraction of particles in class *i* results to [50]:

$$\Delta Q_{0,i} = \frac{\bar{d}_{p,i}^{-3}\,\Delta Q_{3,i}}{\sum_{j=1}^{5} \bar{d}_{p,j}^{-3}\,\Delta Q_{3,j}} \tag{4.3}$$

The particle classes used in this section are summarized in Table 1:

Table 1: Particle size distribution for shear test simulations with Lees-Edwards boundary conditions.

$d_{p,low}$ [μm]	$d_{p,high}$ [μm]	$\bar{d}_p$ [μm]	ΔQ_3	ΔQ_0
5	135	70	0.130	0.940
135	200	167.5	0.065	0.034
200	300	250	0.101	0.016
300	400	350	0.101	0.006
400	1000	700	0.603	0.004

Table 1 shows, that for this wide PSD, the number of particles in the smallest group is 94% of all particles, but they have only a volume fraction of 13% (compared to the overall particle volume). In contrast, more than 60% of the particle volume is held by only 0.4% of all particles. This makes the simulations quite challenging, compared to monodisperse systems.

For the shear tests with Lees-Edwards BC, the Hookean tangential history contact model [25] is used, with the particle properties summarized in Table 2.

---

[1] C. Goniva, personal communication, July 21, 2015

Table 2: Particle properties for shear tests with Lees-Edwards BCs.

Parameter	**Value**
ρ_p[2]	1000 [kg m^{-3}]
Y	$5\cdot10^{6}$ [Pa]
ν_p	0.45
ε	0.1
μ_p	0.1
v_{char}	1 [m s^{-1}]
Bo^*	0, $3.45\cdot10^{-5}$
Δt_{DEM}	$1.6\cdot10^{-7}$ [s]
d_{32}	$2.63\cdot10^{-4}$ [m]
$k_{n,32}$	76.13 [N m^{-1}]

Preliminary results have shown that the vdW cohesion model, in combination with a high coefficient of restitution of the particles, yields unrealistic oscillations during particle-particle contact. To minimize this behavior, a coefficient of restitution of 0.1 is used for the simulations. Such a low coefficient of restitution will not affect the flow behavior in quasi-static flows, which is of primary interest here, and for which the friction coefficient is the main influence parameter.

The simulations are performed for a cohesive system and compared to simulations without cohesion. The particle volume fraction is varied from 0.55 to 0.85, and the final box length is five times the maximum particle diameter in the simulation. The resulting number of particles is between 18,255 and 28,212, depending on the particle volume fraction. The initial domain is compacted by a factor of 0.25 after particle insertion. The simulations are performed for constant dimensionless shear rates $\hat{\dot{\gamma}}$ ranging between $1.43\cdot10^{-4}$ and 0.029. The number of simulation time steps resolving a particle-particle contact is >50 for all particle collisions. For more information on how the time step was calculated, see Luding [24].

---

[2] C. Goniva, personal communication, July 22, 2015.

4.1.3 Results

In this section, the results of the shear test with Lees-Edwards BC are documented. The displayed data consists of the stresses for shear flow at the statistical steady state, and is, of course, time-averaged.

4.1.3.1 Rheology of Polydisperse Particles

In Fig. 3 and Fig. 4 the normal stresses for different particle volume fractions are plotted vs. the applied shear rates for the non-cohesive and the cohesive system, respectively. Without cohesion (Fig. 3) three flow regimes exist: (i) a quasistatic regime for very high solid concentrations, where the stress is proportional to the spring stiffness, and independent of the shear rate, (ii) an inertial regime for dilute systems, where the stress is proportional to the shear rate squared, and (iii) an intermediate regime, where both, the shear rate and the spring stiffness affect the normal stress.

For cohesive systems (Fig. 4), a rate-independent regime bifurcates out of the inertial regime for low shear rates. In this so called, cohesive regime, the inter-particle contact forces exist also for dilute systems (for this wide PSD, a particle volume fraction of 0.75 is already rather “dilute” in the sense that a low stress level develops), because of the cohesion force. When increasing the shear rate, the kinetic stress becomes dominant and the difference between cohesive and non-cohesive systems vanishes. Also, in the quasistatic regime cohesion has no influence on the normal stress, because the particles are permanently in contact. Thus, high stresses exist even for non-cohesive systems.

The results qualitatively agree with those reported by Gu et al. [14] for a monodisperse system. A reason for this qualitative agreement is most likely the high volume fraction of large particles for the PSD used in the present work. Thus, we speculate that the rheology is mainly affected by rather larger particles. Although we have not tested this speculation, we suggest that the rheology might change for different PSDs, and care has to be taken to generalize the above statement.

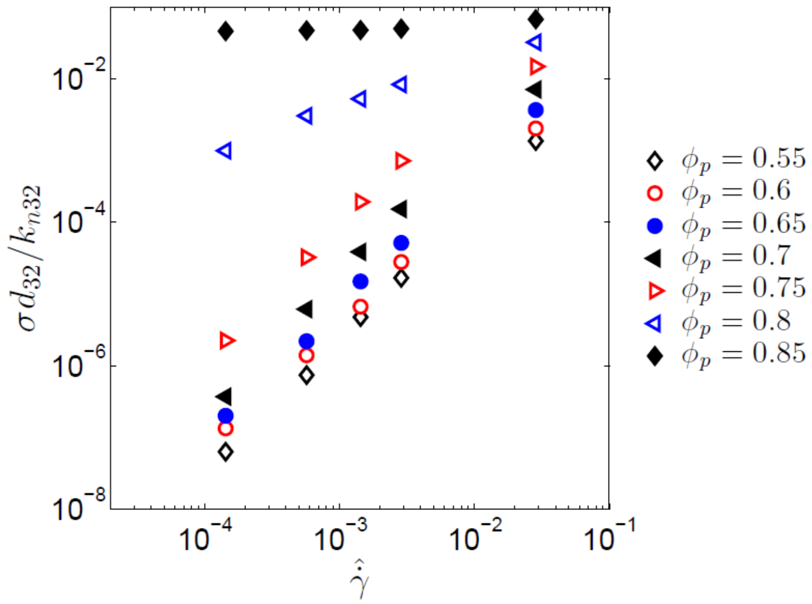

Fig. 3: Scaled pressure vs. scaled shear rate for Hookean contact model without cohesion (*Bo = 0) for different particle volume fractions.**

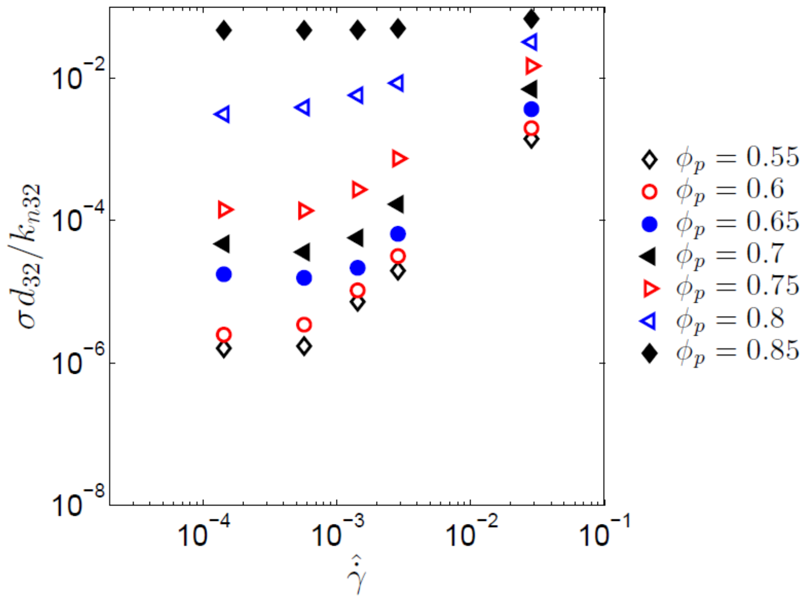

Fig. 4: Scaled pressure vs. scaled shear rate for Hookean contact model with vdW cohesion (*Bo = 3.45·10^{-5}) for different particle volume fractions.**

4.1.3.2 Determination of the Yield Locus

In addition to the rheology at the statistical steady state, the shear tests should also provide the possibility to calibrate the Hamaker constant to the experimentally-determined yield loci of the powder. Thus, we next plot the stresses, i.e. shear and normal stress, against each other. In

Fig. 5 the stresses are shown for the non-cohesive, and the cohesive systems at a dimensionless shear rate $\hat{\dot{\gamma}}$ of $1.4 \cdot 10^{-4}$.

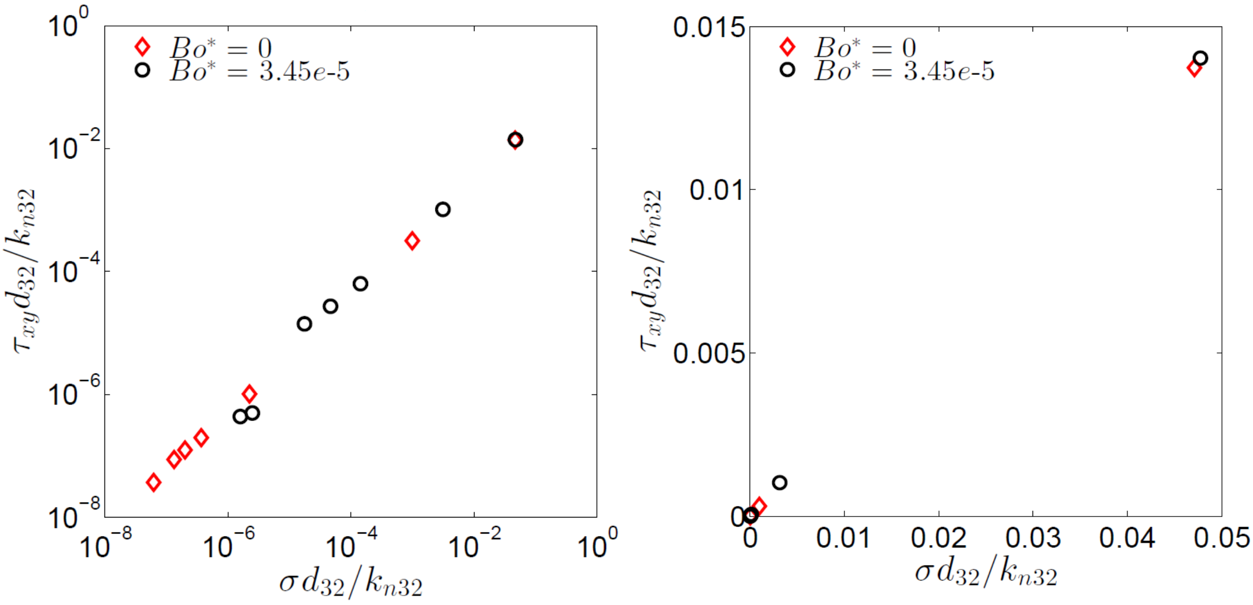

Fig. 5: Scaled shear stress vs. scaled pressure for Hookean contact model and a dimensionless shear rate of $1.4 \cdot 10^{-4}$ (left: logarithmic plot; right: linear plot).

In the quasistatic regime, i.e. for $\phi_p = 0.85$, cohesion does not affect the stresses, but for smaller particle volume fractions, the stresses in cohesive systems are markedly higher than in non-cohesive ones. In the cohesive regime, the shear stress for small particle volume fractions, i.e. for $\phi_p \leq 0.60$, drops off after a certain time of shearing. The reason is that the particles rearrange due to cohesion and shearing, and a “shear plane” is formed. In this shear plane, no particles are located, and hence no stress can develop between the particles.

In this fully periodic setup, the shear stress can only be modified – without changing the Hamaker constant – by changing the inserted particle volume, and thus the normal stress. The problem is that no consolidation of the particles can be applied in this setup. As a consequence, the monitored yield loci for both cohesive, and non-cohesive systems in Fig. 5 (right panel) cannot be distinguished and no macroscopic cohesion can be detected. Thus, we conclude that Lees-Edwards boundary conditions are generally not suitable to measure the yield locus via simulations. Hence, we will now consider a different setup that features a consolidation step.

4.2 Stress Until Shear Setup

As shown in the previous paragraph, simulations in a fully periodic domain cannot provide information about the effect of cohesion on the yield locus. Thus, a new setup was arranged and denoted as the “stress until shear” setup, which is closer to the experimental shear procedure. Most important, our stress until shear setup features a periodic domain, eliminating wall effects completely.

The principle of the stress until shear setup is shown in Fig. 6: The three-dimensional domain is periodic in the shear plane, while this is not the case in the shear gradient direction. In the latter direction, a normal stress is applied to the particle bed via a “symmetric gravity” force, i.e. a consolidation gravitational force. This means that the particle bed is compacted via a gravitational acceleration $\mathbf{g}$, acting on the top half of the particle bed. The bottom half of the particles is pushed upwards to reach exactly zero integral momentum in the domain. Once the particle bed is consolidated, i.e. the normal stress of the particle bed has approached its steady-state value, the desired normal stress is adjusted by setting the gravitational force. After the particle bed is at rest again, an additional gravity in shear direction $\mathbf{g}_{shear}$ is acting on the top particles. Again, the fixed integral momentum leads to an induced motion of the bottom particles in the opposite direction. A more detailed description of the setup will be documented in the next section.

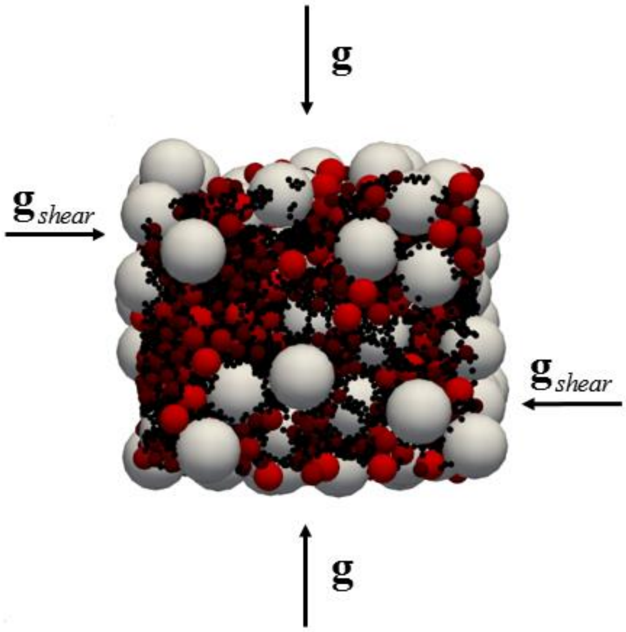

Fig. 6: Principle of the stress until shear setup: Compaction of the bed via a “symmetric gravity” force g, and increasing shear stress via a “shear gravity” $\mathbf{g}_{shear}$.

4.2.1 Test Procedure

In a first step, the particles are randomly inserted in a periodic domain and tri-axially compacted to reach a homogeneous particle sample. Subsequently, the domain size is slightly increased in the shear gradient direction, i.e. in the *y*-direction. Finally, non-periodic boundaries are applied in this direction.

In a next step, the particle sample is consolidated via a “symmetric gravity” force in shear gradient direction. To achieve this, the domain is split into a top region and a bottom region, and a consolidation gravity is applied on the particles in the top region following:

$$\left|\mathbf{g}_{cons}\right| = \frac{p_{cons}\, A_{shear}}{\sum_{i=1}^{N_p} m_{p,i}} \tag{4.4}$$

In this formula, p_{cons} is the consolidation pressure (i.e. an input to the simulation), A_{shear} is the area of the domain in *xz*-direction, and the denominator is the mass of all particles in the domain. By forcing the integral momentum in the domain to zero, the bottom half of the particles is pushed upwards and the particle sample is compacted. The consolidation is finished once the normal stress of the particles σ has approached its steady-state value.

Next, the normal pressure – via the gravitational constant – is reduced to a final value p_{final}. The corresponding gravity $\mathbf{g}_{final}$ is calculated in the same way as above. This brings the huge advantage – compared to experimental devices – that, in this setup, the shear tests can also be performed at zero normal load (or pressure).

After the normal stress of the particles is constant again, additional shear gravity is linearly increased from zero to a maximum value:

$$\left|\mathbf{g}_{shear}^{max}\right| = \frac{p_{shear}^{max}\, A_{shear}}{\sum_{i=1}^{N_p} m_{p,i}} \tag{4.5}$$

This gravity again acts on the top particles, but different to the former ones, it points into *x*-direction, i.e. in shear direction. Thus, each particle in the top region experiences a force in *x*-direction:

$$\mathbf{F}_{shear}(t) = m_p\, \mathbf{g}_{shear}(t) \tag{4.6}$$

The zero overall momentum induces a force on the bottom particles in the opposite direction. In case the acting force on the particles gets larger than the contact force plus – if it exist – the cohesion force, the particles start to move and the sample shears off. This effect can be seen by monitoring (i) the normal stresses originating from contacts σ_{cont}, (ii) the velocity fluctuations σ_{kin}, and (iii) the contact shear stress in *xy*-direction $\tau_{cont,xy}$ (see Appendix A.2 for more information). A typical chronological sequence of the stresses is shown in Fig. 7. In this figure, we have also used a dimensionless time for the stress until shear simulations, which is defined as follows:

$$\hat{t} = t \big/ t_{ref} = t \Bigg/ \sqrt{\frac{d_{32}}{|\mathbf{g}_{cons}|}} \tag{4.7}$$

This scaling of the time has the advantage that the reference time is linearly proportional to the coarse graining ratio, and thus accounts for the longer contact times in coarse-grained systems. The reference time is also proportional to the consolidation pressure and the domain height:

$$t_{ref} \propto CG\sqrt{p_{cons}\, h_{box}} \tag{4.8}$$

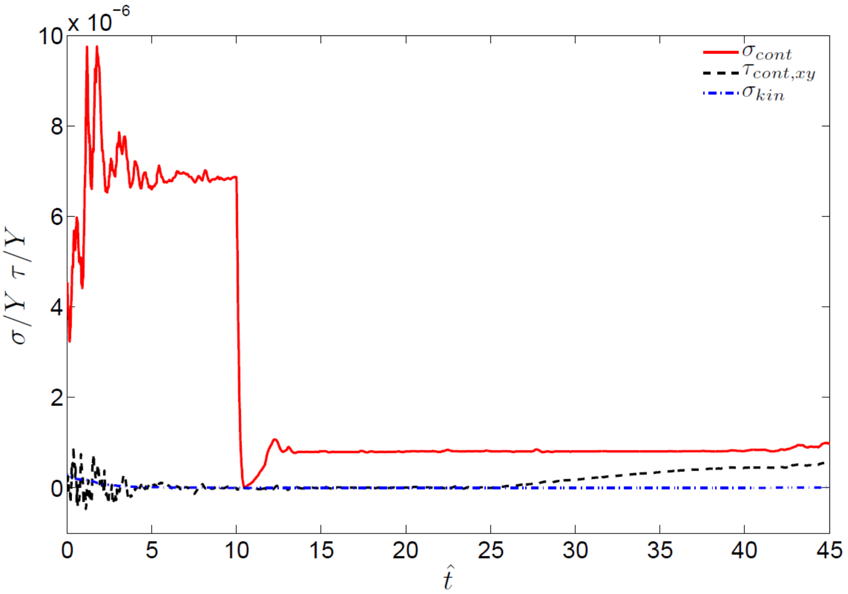

Fig. 7: Scaled stresses vs. dimensionless time for *Bo = 4.36·10^{-7}, *CG* = 1, and $p_{final}/Y = 10^{-5}$. Other parameters are displayed in section 4.2.2.**

4.2.2 Simulation Parameters

For the stress until shear simulations, the Hertz tangential history contact model [25] is used with the following particle properties:

Table 3: Particle properties for stress until shear simulations.

Parameter	Value
ρ_p [3]	1000 [kg m^{-3}]
Y	$5 \cdot 10^6$ [Pa]
ν_p	0.45
ε	0.1
μ_p	0.1
Bo^*	0, 4.36 10^{-9}, 4.36 10^{-8}, 4.36 10^{-7}
Δt_{DEM} [4]	3.9 10^{-7} [s]
d_{32}[5]	$4.25 \cdot 10^{-4}$ [m]

The stiffness-based Bond numbers Bo^* in Table 3 correspond to gravity-based Bond numbers of 0, 10^{-2}, 10^{-1}, and 1 respectively, for a coarse graining ratio of 1 and a gravity of $|\mathbf{g}| = 9.81 m/s^2$. The coefficient of restitution is – again – set to 0.1, to avoid oscillations. The simulation time step is <10% of the Rayleigh time of the smallest particles in the simulation, for more information see [25].

It shall be noted that the uniform volume-based PSD is changed compared to that presented in Chapter 4.1, namely to particle diameters between 30 – 1500µm. This is done to reach the desired minimum fluidization velocity in the segregation tests (see Section 5 for more information). The mean particle diameters of the classes are increased to 100 – 1000µm. Thus, the particle fractions in the classes change slightly as summarized in Table 4.

---

[3] C. Goniva, personal communication, July 22, 2015.

[4] For coarse graining 1. The time step is increased linearly with the coarse graining ratio.

[5] For coarse graining 1. The parcel diameter is linearly proportional to the coarse graining ratio.

Table 4: Particle size distribution for the stress until shear simulations.

$d_{p,low}$ [μm]	$d_{p,high}$ [μm]	$\bar{d}_p$ [μm]	ΔQ_3	ΔQ_0
30	170	100	0.095	0.906
170	300	235	0.088	0.065
300	400	350	0.068	0.015
400	500	450	0.068	0.007
500	1500	1000	0.680	0.006

The simulations are performed with the simulation parameters defined in Table 5.

Table 5: Simulation parameters for the stress until shear simulations .

Parameter	Value
L_{box}[6]	$5 \cdot d_{p,max}$
H_{box}[7]	$5 \cdot d_{p,max}$
N_p	17,557
p_{cons} / Y	10^{-4}
p_{final} / Y	$0, 2\cdot10^{-6}, 5\cdot10^{-6}, 10^{-5}$
p_{shear}^{max} / Y	10^{-5}
$\hat{t}_{cons}$	10
$\hat{t}_{final}$	15
$\hat{t}_{shear}$	20
t_{ref}[8]	$1.72\cdot10^{-3}$ [s]

---

[6] Box length after tri-axial compaction (compaction factor: 0.5, in each direction).

[7] Box height after tri-axial compaction (compaction factor: 0.5); the box height is increased by a factor of 1.5 afterwards.

[8] For coarse graining 1.

The number of particles corresponds to a mean particle volume fraction after compaction of 0.7. The dimensionless times are documented for each subsequent step, so that the whole simulation runs for 45 dimensionless times (without initialization and pre-compaction). Typically, one simulation requires about one hour of computational time on one processor. Thus, these simulations can be done efficiently and without significant limitations on the domain size.

4.2.3 Results

4.2.3.1 Time Averaging Procedure

The data shown in this section are time averaged values, recorded in the limits of:

$$\frac{\sigma_{kin}}{p_{cons}} = 5 \cdot 10^{-6} \div 10^{-5} \tag{4.9}$$

These limits were found to be appropriate to determine the start of “macroscopic shearing” (i.e. bulk particle motion) for most of our simulations. Unfortunately, we could not find a more effective way to detect the onset of “macroscopic shearing”, and also time averaging must be performed over a certain time span to reduce statistical fluctuations.

For the simulations with $p_{final} = 0$ and $CG = 1$, the limits had to be shifted to

$$\frac{\sigma_{kin}}{p_{cons}} = 10^{-5} \div 10^{-4} \tag{4.10}$$

to get more meaningful results (otherwise, the stress ratio was not in the limits, and no averaging was performed). While the selection of these limits must be performed based on visual inspection, we would like to point out that these limits can be easily adapted in post-processing for different particle and simulation properties, if required.

4.2.3.2 Results without Coarse Graining

The yield locus, i.e. the shear stress vs. the normal stress of the particle sample, is plotted for different (stiffness-based) Bond numbers, and final pressures. In a first step, coarse graining is set to one, i.e. particles are un-scaled. The corresponding simulation parameters are defined in Table 5. Each simulation is repeated for three different initial particle configurations.

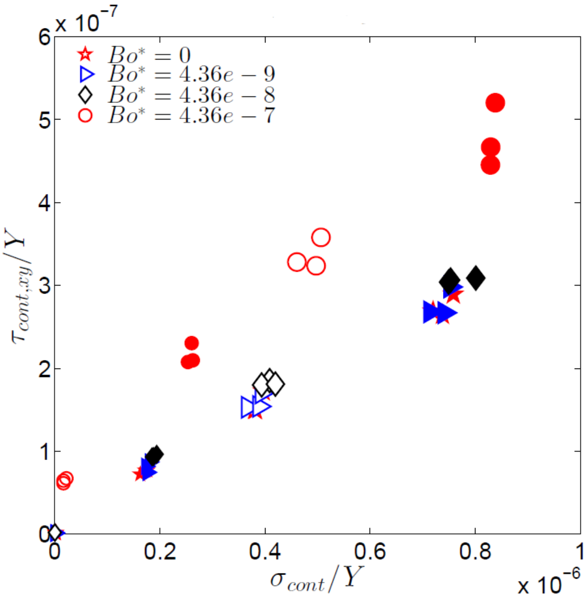

Fig. 8: Scaled shear stress vs. scaled normal stress for different Bond numbers and final pressures, *CG* = 1 for all simulations (consolidation pressure $p_{cons}/Y = 10^{-4}$; $p_{final}/Y = 0$ (small open symbols), $p_{final}/Y = 2\cdot10^{-6}$ (small filled symbols), $p_{final}/Y = 5\cdot10^{-6}$ (large open symbols), and $p_{final}/Y = 10^{-5}$ (large filled symbols)).

The results in Fig. 8 indicate only a weak impact of van der Waals cohesion on the yield locus for small Bond numbers ($Bo^* < 4.36\cdot10^{-8}$). However, with increasing Bond number, the yield locus is shifted to higher shear stresses. Also, without final normal pressure, the shear stress is significantly increased, and thus a clear influence of the Bond number on cohesion, i.e. the intersection with the ordinate of a linear regression of the data, can be observed.

Same as for the fully periodic shear tests in section 4.1, the normal stress increases for large Bond numbers. This effect diminishes – again – for large “external” normal pressures, following to the minor influence of cohesion – compared to the contact forces – in the quasistatic regime.

In Fig. 9, the results of the simulations with cohesion are plotted on a logarithmic scale, and the axes of Fig. 8 are rescaled with the stiffness-based Bond number.

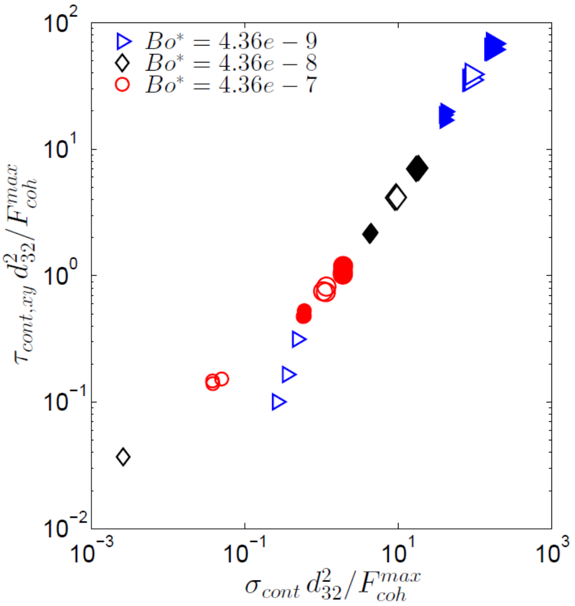

Fig. 9: Shear stress vs. normal stress, scaled with *Bo*/Y*; data for *Bo = 0 excluded, *CG* = 1 for all simulations (consolidation pressure $p_{cons}/Y = 10^{-4}$; $p_{final}/Y = 0$ (small open symbols), $p_{final}/Y = 2 \cdot 10^{-6}$ (small filled symbols), $p_{final}/Y = 5 \cdot 10^{-6}$ (large open symbols), and $p_{final}/Y = 10^{-5}$ (large filled symbols)).**

In Fig. 9, the results with a finite final normal pressure are clustered for a certain Bond number, due to the large difference of the maximum cohesive force. For zero (final) normal load, the detection of macroscopic shear is quite challenging, and needs to be adapted for each simulation. For $Bo^* = 4.36 \cdot 10^{-8}$, for example, two simulations yielded negative results for the normal stress. However, for the sake of automation of the post-processing, this was not considered in this work. Consequently, a certain scatter of the stresses exists for the simulations without normal pressure.

4.2.3.3 Results for Different Coarse Graining Ratios

In a next step, the simulations for $Bo^* = 4.36 \cdot 10^{-7}$ are repeated for coarse graining ratios of 2, 5 and 10, respectively. In these simulations, the total number of particles, and the particle fraction in each class, remained constant. Thus, also the simulation box was enlarged by a fixed factor, i.e. *CG*, in each direction. The other particle properties used are the same as those displayed in Table 3. Preliminary results indicated that the stiffness-based Bond scaling – where the Hamaker constant is linearly proportional to *CG* – yields correct results. The simulation properties remained as documented in Table 5. As mentioned before, the reference time of the simulations increases linearly with *CG*. Thus, the dimensionless times remained constant for all simulations.

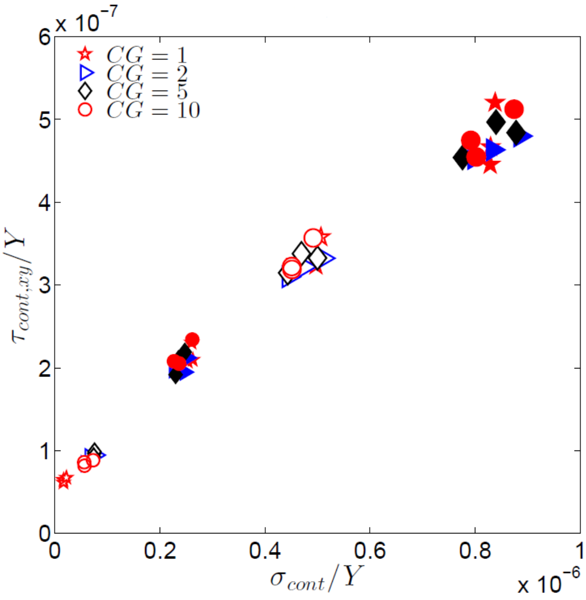

Fig. 10: Scaled shear stress vs. scaled normal stress for different coarse graining ratios and final pressures; *Bo = 4.36·10^{-7}; p_{cons}/Y = 10^{-4}; p_{final}/Y = 0 (small open symbols), p_{final}/Y = 2·10^{-6} (small filled symbols), p_{final}/Y = 5·10^{-6} (large open symbols), and p_{final}/Y = 10^{-5} (large filled symbols).**

In Fig. 10, the results of the simulations for different coarse graining ratios and final normal pressures are summarized. It clearly shows that coarse graining does not influence the yield locus if a stiffness-based Bond scaling is used. The results prove not only that a stiffness-based Bond scaling is correct for the van der Waals cohesion model in dense regimes, but also that the Hertzian contact model is scale invariant. This conclusion is in agreement with the previous work of Bierwisch et al. [21], which considered monodisperse particle ensembles.

Only for zero normal pressure, the stresses in coarse-grained simulations are somewhat higher than for *CG* = 1, but still located on linear yield locus as shown in Fig. 10. We assume that this is due to the adapted limits for the detection of macroscopic shear.

4.2.4 Outlook

The current results provide a sound starting point for future simulations using the stress until shear setup to calibrate the model parameters for experimentally-determined yield loci. The setup presented in this work consists of two regions in which particles are consolidated via a “symmetric gravity” force. Thus, a pressure gradient exists in this direction, meaning that the particles close to the center experience a higher normal pressure than the others. Only in shear direction, the normal stress of the particles is constant. In a next step, this setup could be extended with a center region, where no consolidation gravity acts on the particles, and two bounding regions in which normal and shear forces are applied. Most important, we have been able to demonstrate that the stress until shear setup is superior (with respect to the determination of the yield locus) to the widely-used Lees-Edwards boundary conditions.

5 Fluidized Bed Simulations

In this section, the fluidization behavior of the polydisperse cohesive powder is investigated. For this, the pressure drop and the segregation profiles are numerically investigated in a lab-scale segregation tester (i.e. the one presented by Hedden et al. [7]), using the CFD-DPM approach [21,22]. Additionally, simulations in a smaller periodic domain are performed to reduce the numerical effort. Detailed information about the simulation setup, and the chosen simulation parameters are documented in the following chapters.

5.1 Simulation Setup

The experimental segregation tester setup essentially consists of (i) a cylindrical fluidization column with an expansion chamber on the top, (ii) a fill-chamber assembly to introduce the sample, (iii) a sampling disk assembly to recover samples after the test, and (iv) an air flow controller. The powder is filled into the fluidization column and afterwards fluidized via a defined sawtooth profile. The procedure requires that the air flow rate is systematically increased using a sawtooth profile until the sample is fluidized. The time needed for the whole procedure depends on the flowability of the powder and takes several minutes. Subsequently, the segregated powder is removed from the fluidization column and split into 15-17 equal-sized samples [7].

The numerical setup used in this work has the same dimensions of the fluidization chamber as the experimental segregation tester. Never the less, some restrictions have to be made due to the wide particle size distribution and the large number of particles: (i) the simulation time is limited to two seconds for most simulations, (ii) the filling procedure differs compared to the experiment (the detailed procedure is described later), and (iii) no expansion chamber has been applied for this study. Contrary to the experimental setup, the segregation profiles can be measured directly in the fluidization chamber. Thus, also the temporal progress of segregation can be investigated in our simulation setup.

Additionally to the cylindrical segregation tester setup, a periodic setup with a smaller lateral width has been applied in this study. Detailed information can be found in the next section.

The particle insertion takes place directly in the fluidization column. Afterwards, the particles are compressed via a “fix deform” command (in LIGGGHTS®) to obtain a certain particle volume fraction. An approximately homogeneous powder sample can then be achieved by settling under gravity. The deformation of the simulation box yields a better processor decomposition during settling, and hence shorter simulation time. Fortunately, this artificial deformation of the simulation box does not markedly influence the initial powder sample. Subsequently, the segregation test starts.

The CFD-DPM simulations are performed with the software package CFDEMcoupling®. The coupling between the gas and the particle phase is done via the new "cfdemSolverPimpleImExFace" solver, i.e. a semi-implicit finite volume based PIMPLE algorithm for incompressible particle-fluid suspensions. This solver has the advantage that it uses an algorithm mimicking staggered arrangement of pressure and velocity nodes, which results in a more stable simulation procedure. The temporal discretization (of the coupling forces) is performed using a Crank-Nicolson method, i.e. a second-order accurate semi-implicit formulation. Compared to the prior used "cfdemSolverPimpleImEx" solver, preliminary studies have shown much smoother pressure drop curves with the new solver. Thus, a direct optical detection of the fluidization point is possible in the simulations. The particle-fluid interactions are modeled as the sum of (i) the drag force (i.e. Beetstra monodisperse drag model [27], or Holloway drag model [28]), (ii) the pressure gradient force, and (iii) the viscous force due to the fluid shear stress or deviatoric stress tensor (see Appendix A.1 for more information).

In the numerical setup of the CFD-DPM simulation, a "slip" boundary condition has to be used for the fluid velocity at the cylinder wall. Otherwise (i.e. when using a "fixed value" BC with value 0), the interpolation of the fluid flow yields a wrong estimation of the drag force at the particle position near the wall, and thus, an unrealistic particle behavior. More details about the near wall treatment in Euler-Lagrange simulations can be found in the work of González [51].

5.2 Simulation Parameters

The segregation tests are performed with the same particle size distribution as in the stress until shear simulations in section 4.2.2. The mean particle diameters of the classes are, hence, 100 – 1000µm. The particle properties and the particle size distribution can be found in Table 3 and Table 4. The only difference, compared to the shear tests, is the Bond scaling: While in the shear tests the stiffness-based Bond number was used, preliminary simulations have shown that, for the segregation tests, the gravity-based Bond scaling should be used. Thus the Hamaker constant in the vdW cohesion model is scaled with the coarse graining ratio squared.

The coupling interval between CFD and DEM is 100 for all simulations.

In the following tables the fluid properties and the most important simulation properties for the segregation tests are documented:

Table 6: Properties for air at atmospheric pressure and 20°C [52]**.**

Parameter	Value
ν	$1.511 \cdot 10^{-5}$ [m^2 s^{-1}]
ρ_f	1.205 [kg m^{-3}]

Table 7: Simulation properties for the segregation tests.

Parameter	Value
d_{box}	16 [mm]
h_{box}	210 [mm]
h_{bed}	95 [mm]
CG	1, 1.5, 2
Bo	0, 0.01, 1
$l_{box,in}$	8 [mm]
$N_{cell,in}$	4, 2, 2
$N_{cell,out}$	2, 1, 1
$N_{cell,z}$	105, 70, 52

The simulation domain has a diameter of $d_{box} = 16mm$ and a height of $h_{box} = 210mm$. The particle bed is located 10 mm above the bottom of the CFD domain and has an initial height of approximately $h_{bed} = 95mm$. Due to the rather small column diameter, the simulations are only performed for the coarse graining ratios 1 (i.e. no coarse graining), 1.5 and 2.

In Fig. 11, a top view of the topology of the CFD grid for a coarse graining ratio of 1 is shown.

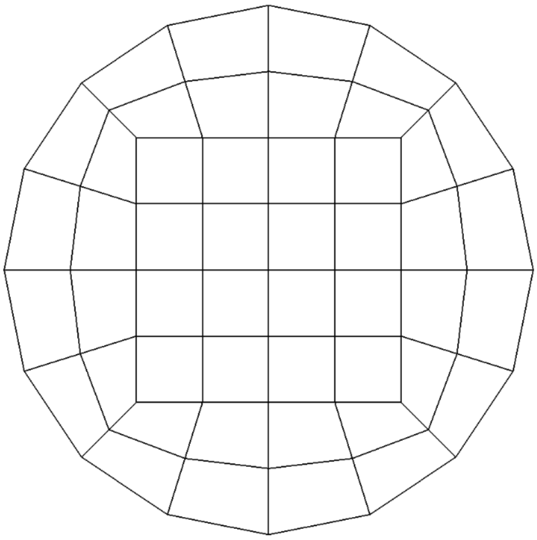

Fig. 11: Top view on the CFD grid in the cylindrical setup for coarse graining 1.

The CFD grid consists of an inner quadratic section with a side length of $l_{box,in} = 8mm$ and an outer section. The number of cells in radial direction (i.e. $N_{cell,in}$ and $N_{cell,out}$) and in vertical direction (i.e. $N_{cell,z}$, equally distributed over the height) for the different coarse graining ratios are documented in Table 7. The minimum cell size is at least two times the maximum particle (or parcel) diameter for all simulations.

The periodic segregation tester setup is made out of the inner quadratic section of the cylindrical setup. Thus, the size and the number of CFD cells are also equal to the inner section.

The number of particles in the cylindrical setup is approximately 3 Mio, 900,000 and 380,000 for the coarse graining ratios 1, 1.5 and 2, respectively. In the periodic setup the number of particles is approximately 960,000, 290,000 and 120,000 for the coarse graining ratios 1, 1.5 and 2, respectively. The simulation domain is decomposed into up to 128 processors.

As mentioned in the previous section, the fluidization procedure in this work differs from the experimental procedure proposed in Hedden et al. [7]. Unless otherwise noted, the superficial fluid velocity is linearly increased from zero to a final value of $U_0 = 9\,mm/s$ (i.e. 1.5 times the desired minimum fluidization velocity of $U_{mf} = 6\,mm/s$[9]) within 0.1 s and held constant for 1.7 s. Subsequently, the fluid velocity is linearly decreased to zero within 0.2 s. Thus, the

---

[9] C. Goniva, personal communication, July 21, 2015.

overall runtime of the CFD-DPM simulation is 2 s. The fluid is homogeneously distributed over the lateral width at the inlet, i.e. it has a block profile.

5.3 Results

All simulations in this section are performed with gravity-based Bond scaling, i.e. the Hamaker constant scales with $Ha \propto CG^2$.

5.3.1 Pressure Drop and Minimum Fluidization Velocity

First, the fluidization curves are investigated for the different Bond numbers and coarse graining ratios. To achieve this, the pressure drop and the superficial fluid velocity are recorded. The pressure drop is scaled with a reference pressure drop defined as

$$p_{ref} = \frac{\sum_{i=1}^{N_p} m_{p,i} \left|\mathbf{g}\right|}{A\rho_f} \tag{5.1}$$

and is about $p_{ref} = 611 Pa$ for all simulations.

The fluidization curves in the periodic setup with the Beetstra monodisperse drag law [27] are as follows:

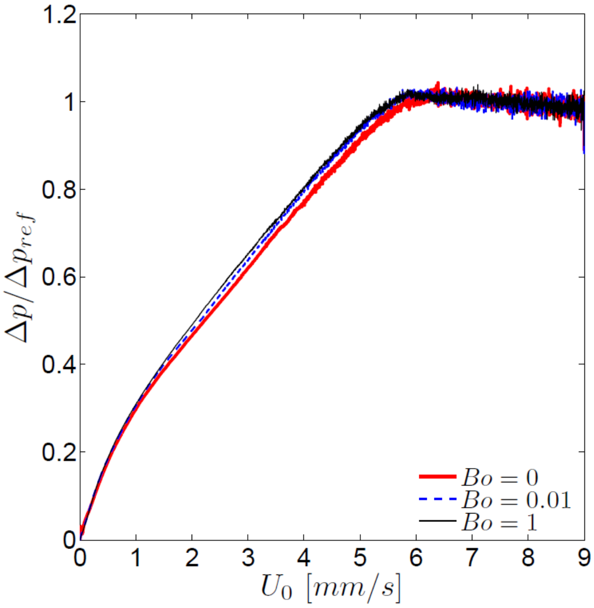

Fig. 12: Fluidization curve for different Bond numbers and *CG* = 1 in the periodic setup.

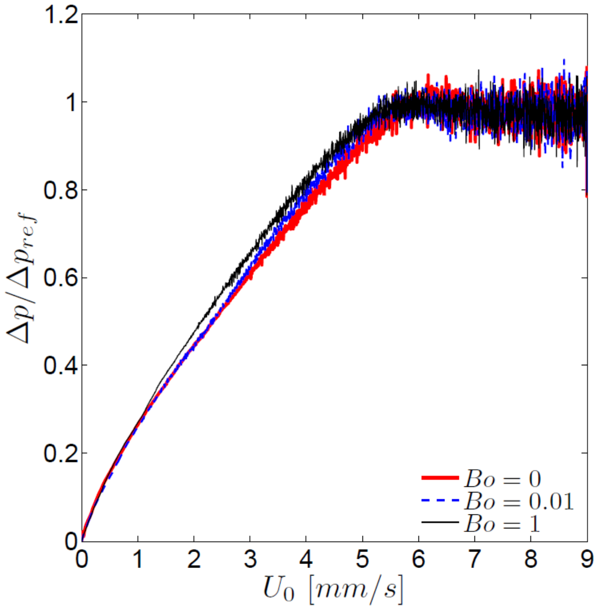

Fig. 13: Fluidization curve for different Bond numbers and *CG* = 1.5 in the periodic setup.

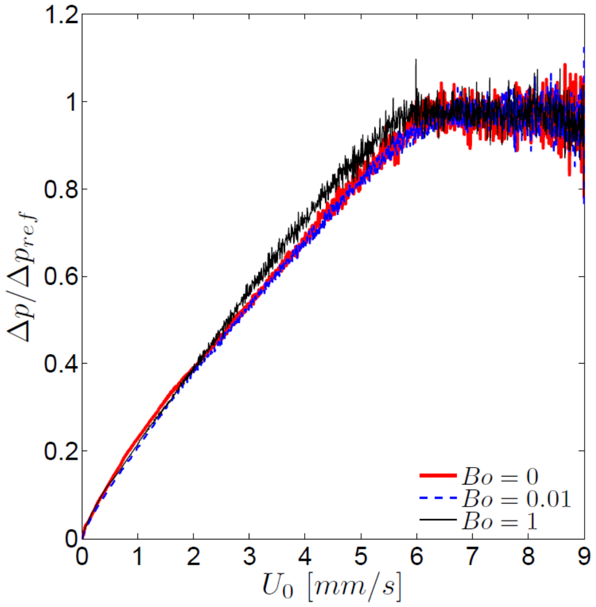

Fig. 14: Fluidization curve for different Bond numbers and *CG* = 2 in the periodic setup.

The fluidization curves in the periodic setup (i.e. Fig. 12 to Fig. 14) indicate, that cohesion only marginally influences the shape of the curve and the minimum fluidization velocity. The fluctuations of the pressure drop are larger in the coarse-grained simulations. It may be assumed that this is due to the relatively large parcel size, compared to the width of the domain. The figures show a decrease of the slope of the pressure drop at a fluidization velocity of about $U_0 = 1 mm/s$. This decrease is found to be characteristic for most of the simulations in this study. We speculate that the decrease of the pressure drop originates from a rearrangement of the small particles.

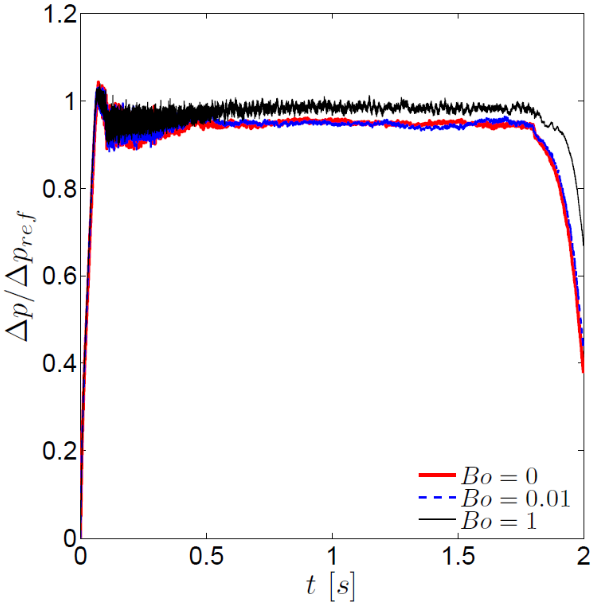

Fig. 15: Pressure drop vs. time for different Bond numbers and *CG* = 1 in the periodic setup.

In Fig. 12 to Fig. 14 no overshoot of the pressure drop can be seen at the fluidization point in the periodic setup. However, when plotting the temporal progress of the pressure drop (as shown in Fig. 15), a decrease of the pressure drop occurs after the initial fluidization, i.e. the rapid increase of the fluidization speed within the first 0.1 s. Consequently, the final value for the pressure drop (at t = 1.8 s) is slightly below the reference pressure drop. Qualitatively, this behavior can be observed for all investigated coarse graining ratios and Bond numbers. For the simulations with coarse graining, the pressure drop fluctuations at the beginning are slightly larger (data not shown).

Next, the fluidization curves in the cylindrical setup, again, with the Beetstra monodisperse drag law [27], are investigated.

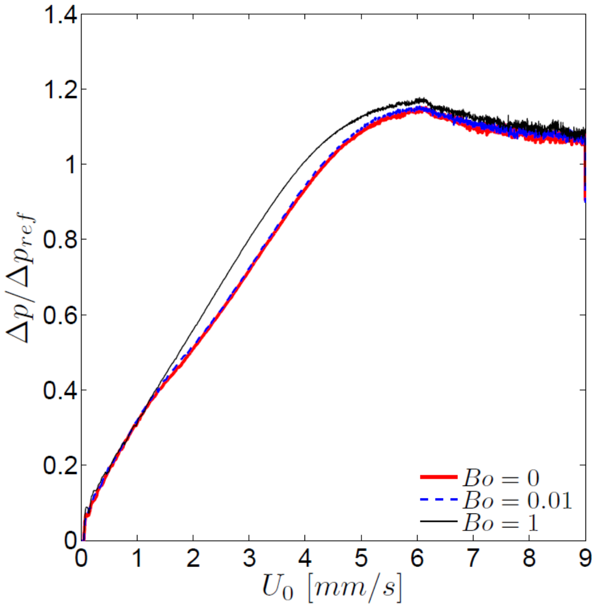

Fig. 16: Fluidization curve for different Bond numbers and *CG* = 1 in the cylindrical setup.

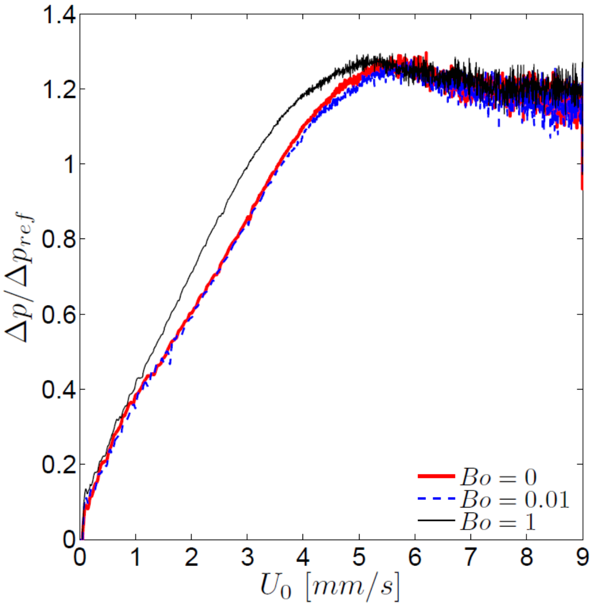

Fig. 17: Fluidization curve for different Bond numbers and *CG* = 1.5 in the cylindrical setup.

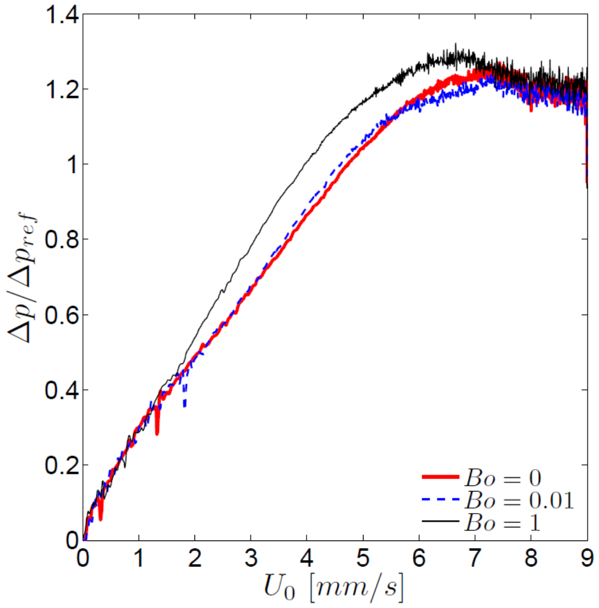

Fig. 18: Fluidization curve for different Bond numbers and *CG* = 2 in the cylindrical setup.

In the cylindrical setup, the influence of the Bond number on the fluidization curves (cf. Fig. 16 to Fig. 18) is larger than in the periodic setup. For example, for high Bond numbers no decrease of the slope of the fluidization curves exists at fluidization velocities between approximately 1.5 and 6 mm/s. The pressure drop overshoots at U_{mf} and decreases slowly to the final (reference) value for all simulations. This behavior cannot be observed for the periodic setup and becomes more pronounced with increasing coarse graining ratio. Thus, we assume that the overshoot is due to wall effects, following the line of thoughts documented in Jackson [53]. Same as for the periodic setup, the fluctuations of the pressure drop become larger with increasing coarse graining ratio.

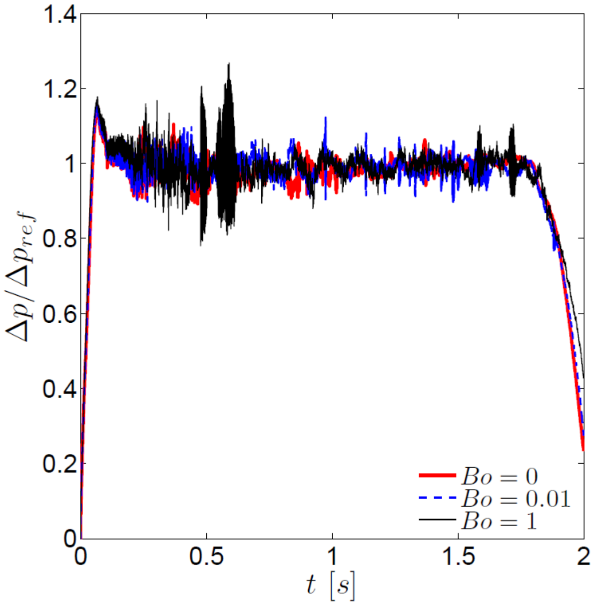

Fig. 19: Pressure drop vs. time for different Bond numbers and *CG* = 1 in the cylindrical setup.

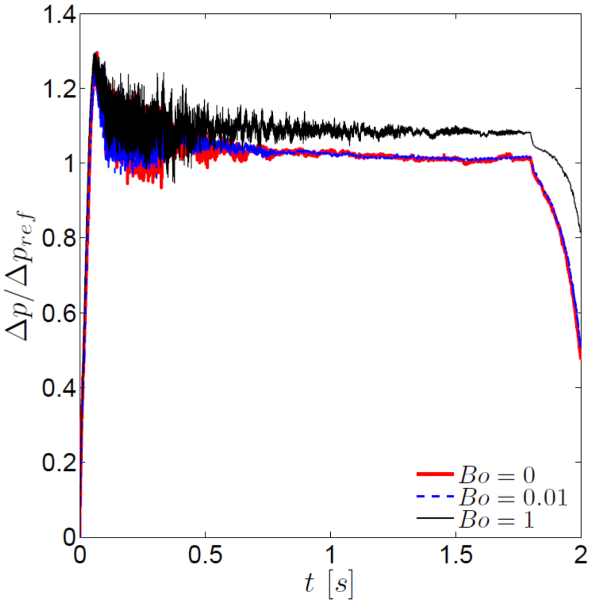

Fig. 20: Pressure drop vs. time for different Bond numbers and *CG* = 1.5 in the cylindrical setup.

In Fig. 19 and Fig. 20, the temporal progression of the pressure drop is shown for coarse graining 1 and 1.5, respectively. With coarse graining, the pressure drop for high Bond numbers is higher than the reference value. For *CG* = 2, the temporal progress is qualitatively similar to Fig. 20. These results indicate that the influence of cohesion in the coarse-grained systems is too high if gravity based-scaling is used. Again, we assume that this is due to (unwanted) wall effects that appear in coarse graining, since the cylinder diameter-to-parcel diameter becomes smaller with increasing CG.

When using the Holloway drag model [28] the minimum fluidization velocity is about $U_{mf} = 13 mm/s$, i.e. significantly larger. The pressure drop at fluidization lies – same as for the Beetstra monodisperse drag model [27] in the periodic setup – within the range of the reference pressure drop. Due to the huge difference of the minimum fluidization velocity for the drag models, and the maximum diameter ratio of 1:2.5 used in Holloway et al. [28], we focus on the Beetstra monodisperse drag model in this work. Moreover, in preliminary studies, the Holloway drag model [28] was found to be sensitive to numerical parameters as long as the grid size was in the range of the maximum particle diameter. We speculate that this is due to the additional need for reconstructing the local Sauter mean diameter in the Holloway drag model.

5.3.2 Segregation Profiles

Segregation profiles are measured based on the experimental segregation tester (as described in Hedden et al. [7]). The experimental device provides about 16 equally sized samples of the powder in vertical direction. This corresponds to a height of one sampling bin of about 6 mm in the tester. In this section, the Sauter mean diameter of the particles in each bin (i.e. $d_{32,bin}$) is compared to the Sauter mean diameter d_{32} of the whole particle ensemble. This is contrary to the work of Hedden et al. [7], who measured the median diameter of their powder samples.

5.3.2.1 *Segregation Profiles with the Beetstra Monodisperse Drag Law*

In this section, the segregation profiles of the simulations with the Beetstra monodisperse drag law [27] are documented. The results indicate that the calculated Sauter mean diameter in the bins fluctuates, and no clear trends can be observed. Thus, the averaging was also done over two and three bins in the post processing in order to smoothen out these fluctuations.

In a first step, the influence of the Bond number is investigated for coarse graining ratios in the cylindrical setup. The small symbols, connected through dotted lines, indicate the initial – not segregated – profile, and the large symbols, connected through solid lines represent the final segregation profile after 2 seconds of simulation.

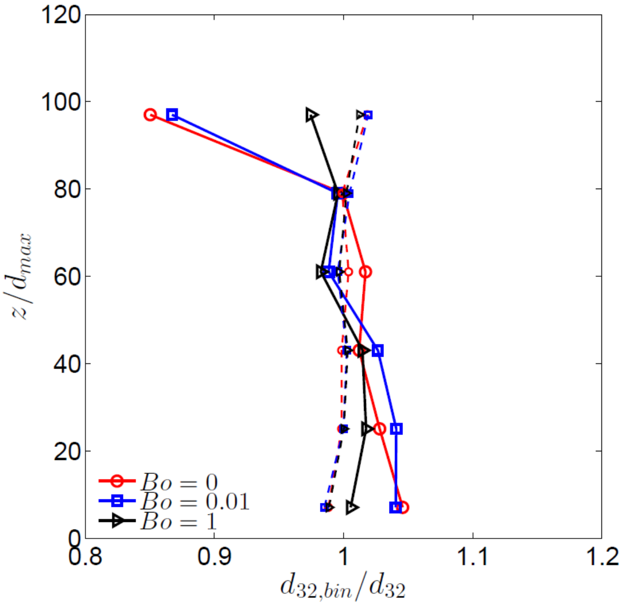

Fig. 21: Segregation profiles for different Bond numbers and *CG* = 1 in the cylindrical setup (averaged over three bins).

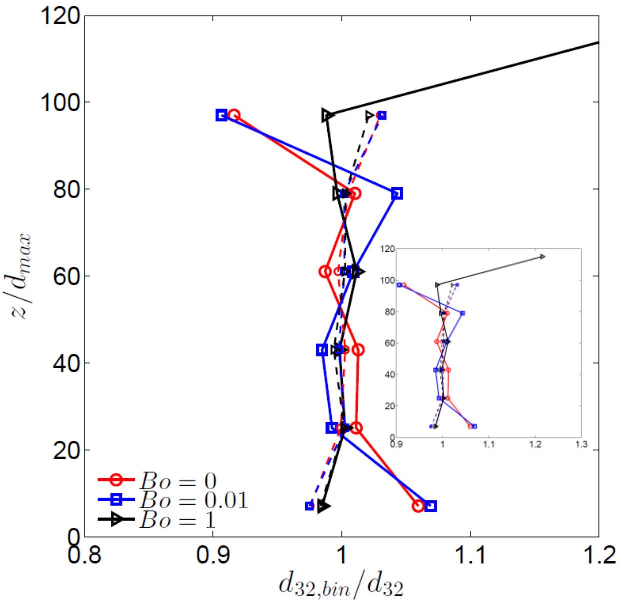

Fig. 22: Segregation profiles for different Bond numbers and *CG* = 1.5 in the cylindrical setup (averaged over three bins).

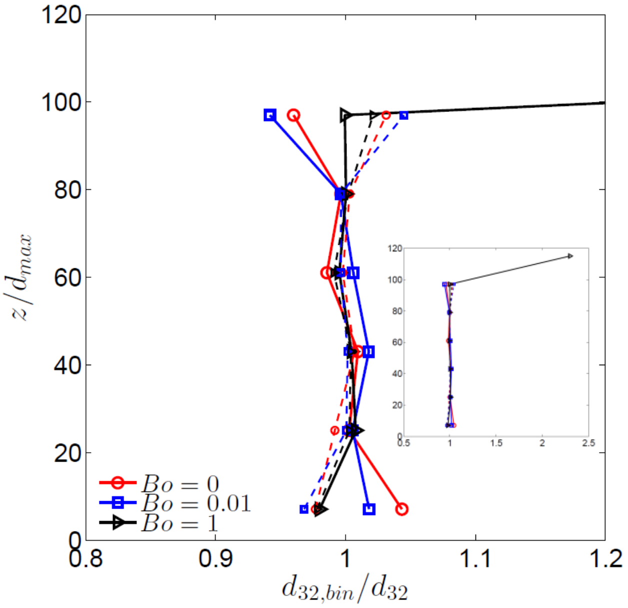

Fig. 23: Segregation profiles for different Bond numbers and *CG* = 2 in the cylindrical setup (averaged over three bins).

Fig. 21 to Fig. 23 show the segregation profiles for the simulations in the cylindrical setup. In general, the segregation tendency of the powder can be seen. The small particles rise upwards through the powder. Thus, the mean particle diameter in the bottom bins increases, and the small particles accumulate in the upper bins.

In Fig. 22 and Fig. 23, the profiles for $Bo = 1$ indicate a steep increase of the mean particle size in the top bin. The reason is that an accumulation of a few, mainly larger particles is formed during the simulation, which penetrates into the top bin. Hence, statistically speaking, those are weak data points, since the number of particles in the top bin is very low. However, for the sake of simplicity, the number of particles in each averaging bin is not accounted for in those plots.

The influence of the Bond number on the segregation tendency of the powder can be seen for all coarse graining ratios. While segregation occurs in the simulations without cohesion, and with only weak cohesion (i.e. $Bo = 0.01$), it is nearly suppressed for the larger Bond numbers (i.e. $Bo = 1$). Without coarse graining, some segregation occurs even for $Bo = 1$ (see Fig. 21). This is not the case for the coarse-grained simulations (Fig. 22 and Fig. 23). The reason can be either (i) that the gravity-based Bond scaling overestimates the cohesion, or (ii) that boundary effects influence the coarse-grained simulations. The latter speculation is supported by our results from simulations without cohesion, since the Sauter mean diameter in the top bin increases along with a rising coarse graining ratio.

In a next step, the simulations are repeated in the periodic domain, with a lateral width of $l_{box} = 8mm$. The results are shown in Fig. 24 to Fig. 26.

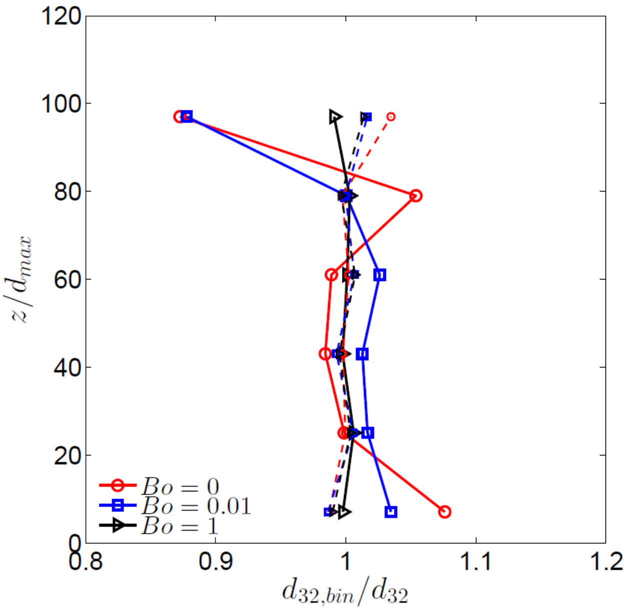

Fig. 24: Segregation profiles for different Bond numbers and *CG* = 1 in the periodic setup (averaged over three bins).

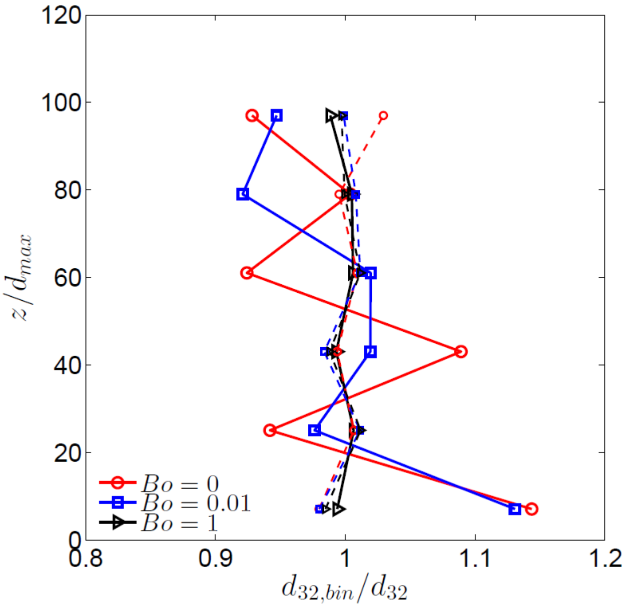

Fig. 25: Segregation profiles for different Bond numbers and *CG* = 1.5 in the periodic setup (averaged over three bins).

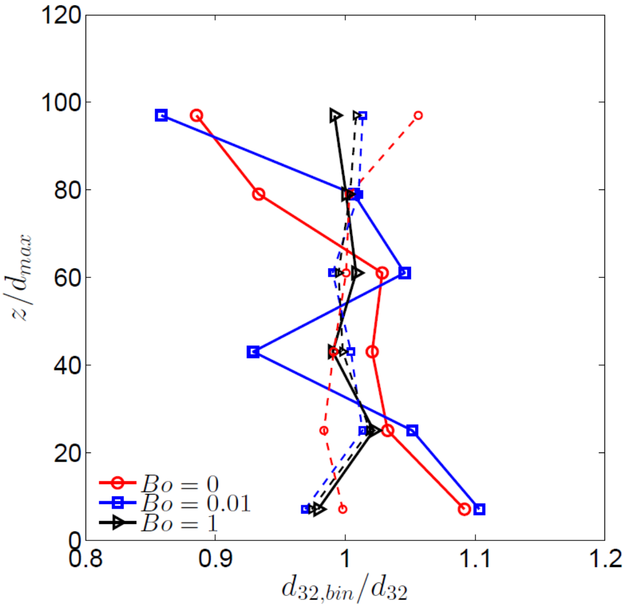

Fig. 26: Segregation profiles for different Bond numbers and *CG* = 2 in the periodic setup (averaged over three bins).

Same as in the cylindrical setup, the influence of the Bond number on the segregation of the powder can be seen in the periodic setup (i.e. in Fig. 24 to Fig. 26). For $Bo = 1$, segregation is suppressed even without coarse graining (Fig. 24). The smaller lateral width of the periodic domain leads to more fluctuations of the Sauter mean diameter in the bins for the less cohesive powders. The results indicate that the small particles form clusters when they move through the fluidized powder bed. Nevertheless, the simulation time of two seconds is too short to allow detailed information about the observed clustering phenomenon.

In a next step, the temporal progress of segregation is investigated. Therefore, the non-cohesive simulation of Fig. 26 – in the periodic setup, with $CG = 2$ and $Bo = 0$ – is repeated for a longer run time and snapshots are taken in periodic intervals.

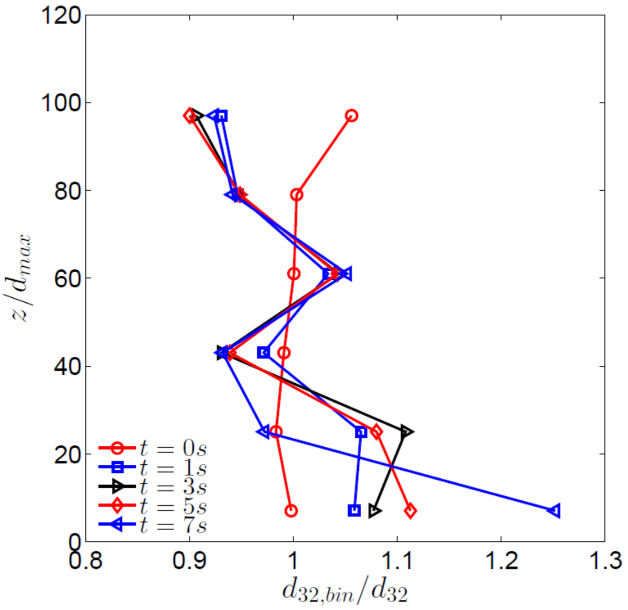

Fig. 27: Temporal progress of the segregation profile for *Bo* = 0 and *CG* = 2 in the periodic setup (averaged over three bins).

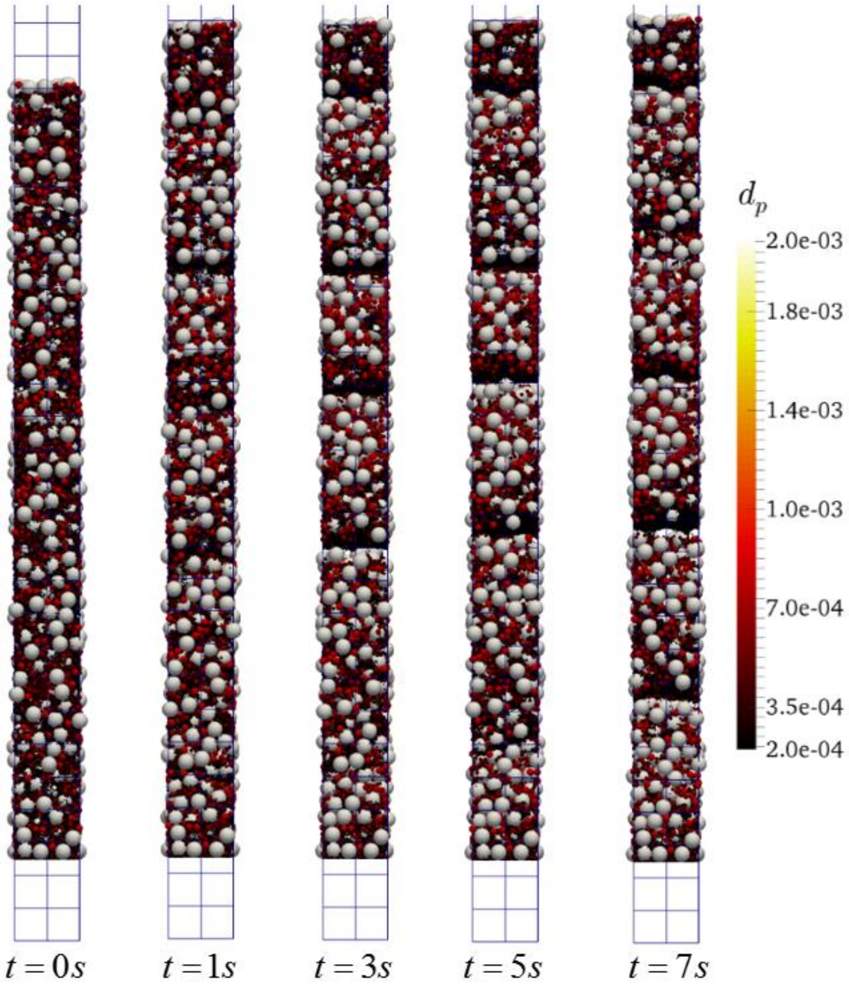

Fig. 28: Snapshots of the particles at the beginning, and after different times of simulation (periodic setup, *Bo* = 0 and *CG* = 2).

Fig. 27 and Fig. 28 show the segregation trend due to fluidization for a non-cohesive powder. It can be clearly seen that the initially homogeneously distributed powder forms clusters – or layers – of small particles in the early stage of fluidization. These particle clusters subsequently move slowly upwards through the bed. The segregation profiles indicate an ongoing segregation in the bottom region of the bed, while in the top half of the particle bed, the Sauter mean diameter in the bins remains more or less unchanged between 1 and 7 seconds of simulation.

Additionally, the bed expansion during fluidization shown in Fig. 28 is about 10% of the initial bed height. This value was found to be approximately constant for all the simulations in this study. Thus, the domain height of the simulations can be reduced in future simulations to improve processor utilization and reduce computational time.

Subsequently, the influence of the lateral width of the periodic domain is investigated. To do this, the box length and the number of CFD cells in *x*- and *y*-direction are doubled to

$l_{box} = 16mm$ and $N_{cell,xy} = 4$, respectively. The coarse graining ratio is again set to 2 for the non-cohesive powders. The fluidization ramp and the other parameters are taken from Section 5.2.

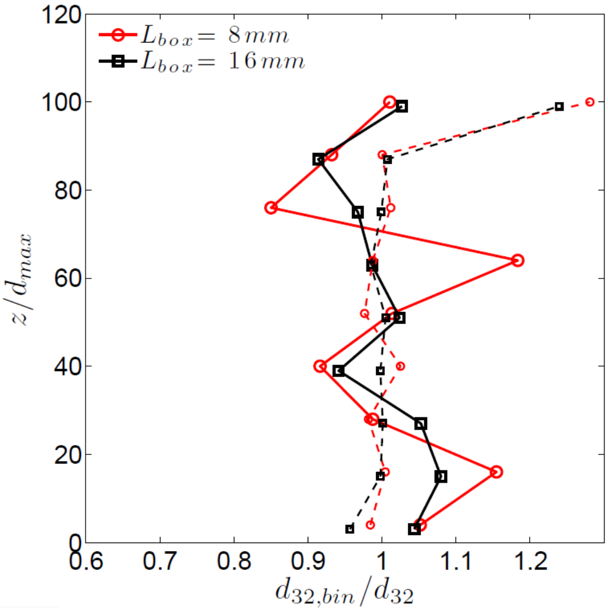

Fig. 29: Segregation profiles for different lateral widths of the periodic domain for *Bo* = 0 and *CG* = 2 (averaged over two bins).

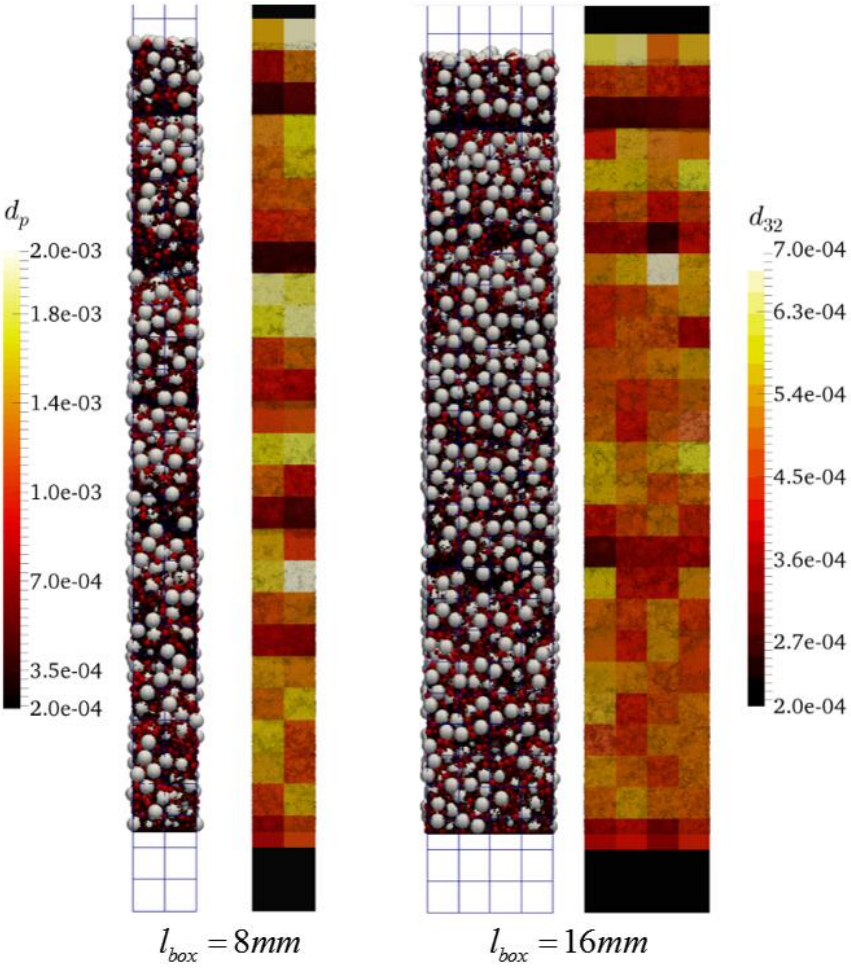

Fig. 30: Snapshots of the particles and the Sauter mean diameter in the CFD cells at the end of the simulations for different lateral widths of the periodic domain (*Bo* = 0 and *CG* = 2).

In Fig. 29, the segregation profiles for the two simulations are displayed (averaged over two bins). While the initial profiles are almost identical, the segregation profile at the end of the simulation in the wider domain fluctuates less than the other. This is in agreement with the results displayed in Fig. 30, where the snapshots of the particles and the information of the Sauter mean diameter in the CFD cells are shown. In the narrow domain, one can clearly see the layers of small particles. In the wider domain, only one distinct layer has formed at the top of the particle bed. Within the bed, also some smaller clusters exist, but the overall particle distribution is more homogeneous compared to the narrow domain.

This leads us to the conclusion, that in the narrow periodic domain, the parcel diameter is too large compared to the lateral domain width. Thus, segregation is strongly affected, and simulations of the narrow domain lead to an amplification of segregation layers in the powder. Nevertheless, simulations in the narrow periodic domain can be used to – more or less – quickly determine the influence of the Bond number on segregation.

As mentioned in Section 5.2, the length of the CFD cells was fixed to be two times the maximum particle – or parcel – diameter for all simulations. Thus, we want to investigate the influence of the CFD grid size on the segregation of the powder. To do this, the length of the CFD cells in vertical direction $l_{cell,z}$ is increased and the simulation in the periodic setup for $CG = 2$ and $Bo = 0$ is repeated. All other parameters remain as defined in section 5.2.

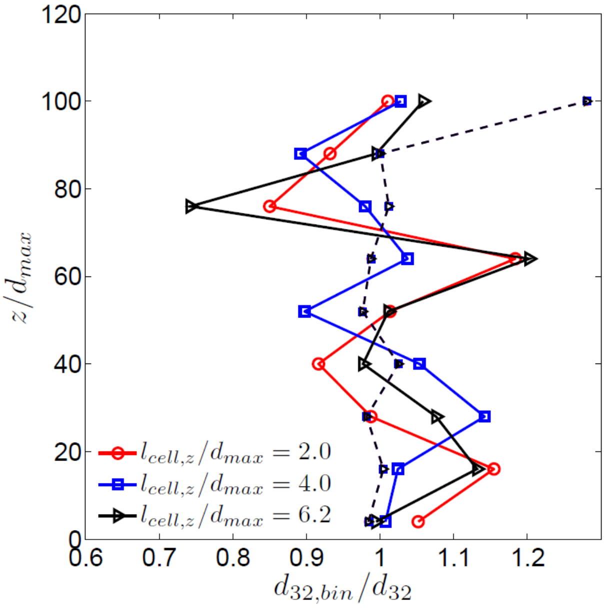

Fig. 31: Segregation profiles for different numbers of CFD cells in the periodic domain for *Bo* = 0 and *CG* = 2 (averaged over two bins).

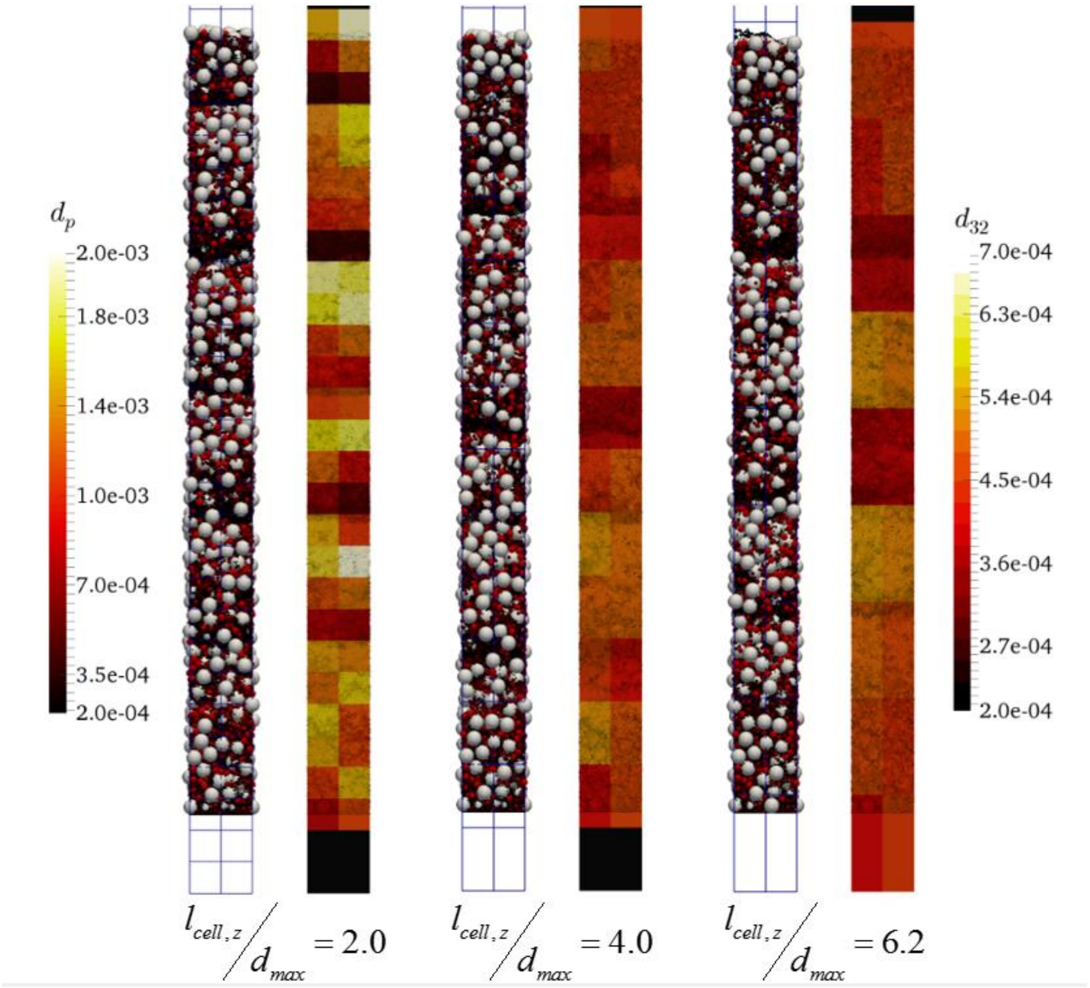

Fig. 32: Snapshots of the particles and the Sauter mean diameter in the CFD cells at the end of the simulations for different numbers of CFD cells in the periodic domain (*Bo* = 0 and *CG* = 2).

In Fig. 31 one can see that these tests are performed with the identical initial particle sample. Merely the different CFD grid size (i.e. the grid size in vertical direction was doubled and approximately tripled, respectively) yields quite different segregation profiles at the end of the simulations. The reason can be seen in Fig. 32: The larger CFD cells lead to larger spaces between the layers of small particles. We speculate that this is caused by the more homogeneous exchange fields between CFD and DEM (i.e. particle concentration, and coupling forces) if larger cells are used. Thus, the fluid-particle drag fluctuates less and the smaller particles build larger clusters, compared to the simulation with the finer grid. One possibility to overcome these fluctuations would be a so-called smoothing model in CFDEM®, but preliminary results showed that the currently implemented model cannot be used for such dense systems. The issue with smoothing is that the drag coefficient at extremely high particle concentrations is very sensitive to changes in the local particle volume fraction. Thus, smoothing near the free surface (i.e. at the very bottom and top of the powder bed) leads to a tremendous change in the drag coefficient, and hence the required fluid speed to induce fluidization.

5.3.2.2 Comparison between the Beetstra monodisperse and Holloway Drag Law

For the sake of completeness, the Beetstra monodisperse drag correlation [27] should be compared to the Holloway drag model [28] for polydisperse gas-solid suspensions. Additionally, the Beetstra monodisperse drag model [27] is also expanded with the force sub-model “ImExCorr” in CFDEM®. This force sub model changes the character of the force mapping on the fluid side, however, does not change the overall force that is mapped. Details about the models can be found in Appendix A.1. The results are shown in Fig. 33 to Fig. 34:

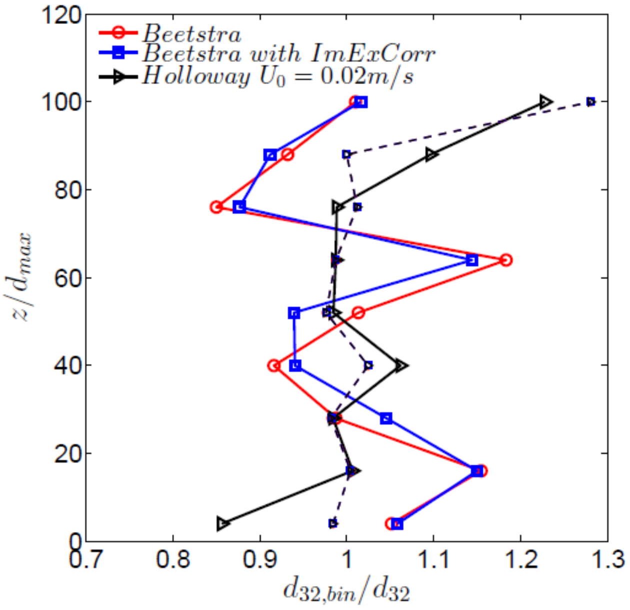

Fig. 33: Segregation profiles for different drag models in the periodic domain for *Bo* = 0 and *CG* = 2 (averaged over two bins).

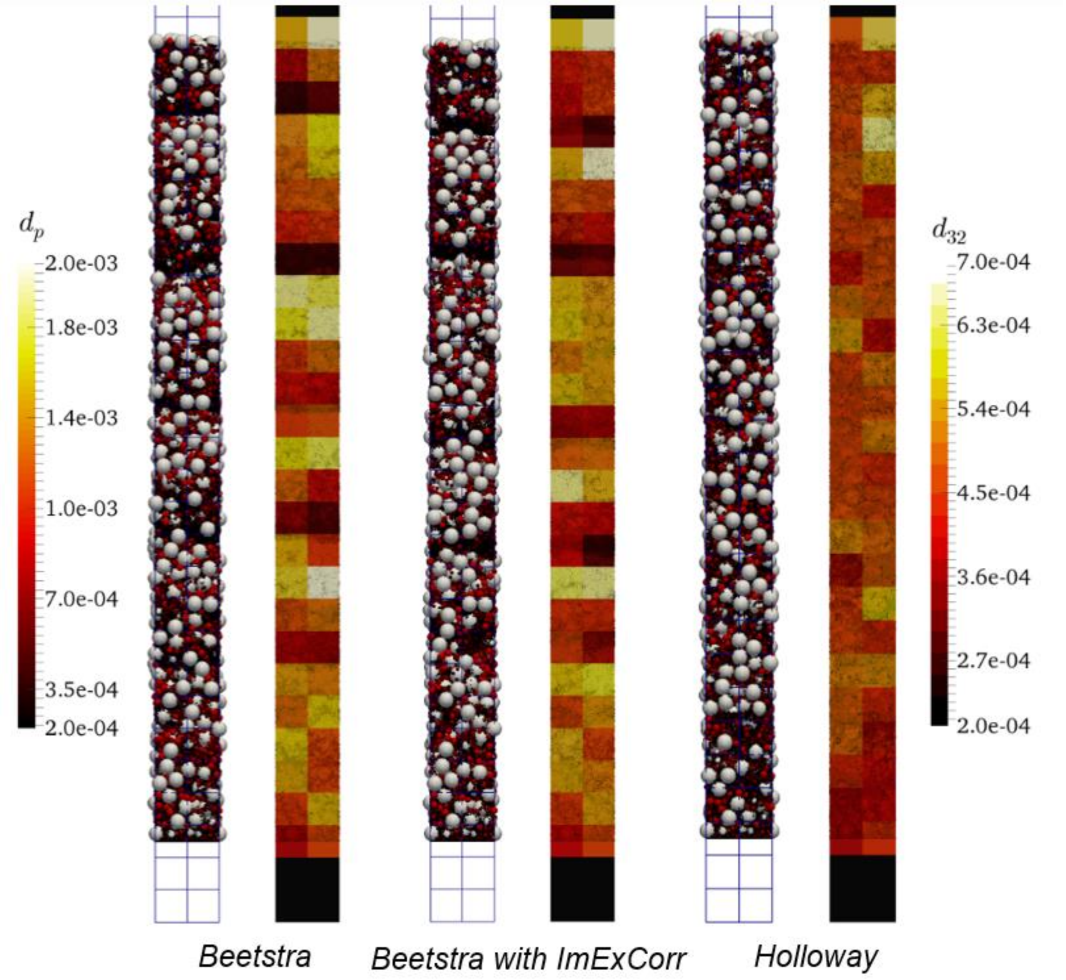

Fig. 34: Snapshots of the particles and the Sauter mean diameter in the CFD cells at the end of the simulations for different drag models in the periodic domain (*Bo* = 0 and *CG* = 2).

Due to the higher required minimum fluidization velocity U_{mf} for the Holloway drag model [28] (see section 5.3.1), the superficial gas velocity was increased to $U_0 = 20\,mm/s$ in this case to provide identical fluidization conditions for all simulations.

The segregation profiles in Fig. 33 indicate only small differences between the simulation with the Beetstra monodisperse drag model [27] used in this work, and the one with the force sub-model “ImExCorr”. Also, the particle patterns in Fig. 34 do not result in marked differences when using the sub model.

Contrary to the Beetstra monodisperse drag model [27], segregation is almost completely suppressed with the Holloway drag model [28]. Surprisingly, small particles seem to accumulate to a certain extent in the bottom region when using the Holloway drag model. Also the particle pattern stays nearly homogeneous.

This is in agreement with other authors who were unable to obtain consistent results with the Holloway drag model [28] for bi-disperse [51] and polydisperse dense flows [54], respectively.

6 Conclusion

In the present work, a workflow for the simulation of segregation profiles in a lab-scale segregation tester [7] was developed and applied to a cohesive polydisperse powder mixture. The simulations were performed for spherical particles with a maximum size ratio of 10, and a uniform (volumetric) size distribution. To allow efficient simulations, a van der Waals cohesion force model [33] was introduced into LIGGGHTS®, a highly parallel granular dynamics code. The core tool in the developed workflow is the calibrated CFD-DPM, i.e. a parcel-based simulator for dense gas-particle suspensions. While the base model was already fit for the parcel-based approach [21,22], the scalability of the van der Waals cohesion model was investigated within this study. The scaling is based on two dimensionless Bond numbers: (i) a gravity-based Bond number [16], where the van der Waals cohesion model scales with the coarse graining ratio squared, and (ii) a stiffness-based Bond number [14], where the cohesion model is linearly proportional to coarse graining for both the Hertzian and the Hookean contact law available in LIGGGHTS®. It has to be mentioned that, within this work, a constant minimum surface distance for the van der Waals cohesion model was used. Other groups also used a particle size dependent minimum surface distance (e.g. $s_{min} = 4 \cdot 10^{-5} d_p$, [14]). This yields to a stronger dependency of the cohesion force on the particle's diameter, and thus to other scaling rules for parcel-based simulations.

Simulations were performed in a three-dimensional periodic shear setup with Lees-Edwards boundary conditions [49] to investigate the influence of cohesion on the granular rheology of dense polydisperse granular materials. While the three classical flow regimes (quasistatic, inertial, and intermediate) persist for non-cohesive granular materials, a new rate-independent regime bifurcates out of the inertial regime for cohesive particles. These findings are in qualitative agreement with those for monodisperse flows [14]. Nevertheless, the influence of cohesion on the yield locus cannot be determined when using Lees-Edwards boundary conditions. Thus, a novel "stress until shear" setup was developed. In this three-dimensional setup, a particle bed is compacted under "symmetric gravity" conditions to reach a certain normal (consolidation) stress. Subsequently, the normal stress is reduced to a final value, and an additional gravity in shear direction is induced until the particle bed shears off. The stress until shear setup brings advantages compared to other simulation methods and common experimental devices [11–16,48,55,56]. Namely, (i) direct access to the (cohesive) shear stress at zero normal load, (ii) no influence of wall effects, and (iii) no influence of shear gradients due to rotation exist in this setup. The presented simulation results indicate a clear influence of cohesion on the yield locus, demonstrating the suitability of our approach. The dimensionless stiffness-based Bond number can be interpreted as a characteristic cohesive force normalized with a characteristic contact force [14]. Fig. 9 shows that simulation results collapse to a single line when the stresses are scaled with the maximum cohesion force and a characteristic length. Only the results of simulations without final normal load scatter. Furthermore, results indicate no influence of coarse graining on the yield locus for stiffness-based scaling of the cohesion model.

Subsequently, fluidization tests in a periodic setup, as well as in a (cylindrical) lab-scale segregation tester setup [7] were performed. In a first step, the minimum fluidization velocity U_{mf}, and the influence of the Bond number was determined for coarse graining ratios of 1, 1.5, and 2. Unfortunately, due to the small cross-sectional area of the simulation setup, larger coarse graining ratios could not be investigated. The main reason is the limitation in the computation time, which restricts us to typically $< 10^6$ particles in a typical simulation. In summary, segregation tests with up to 3 Mio. particles were performed with about 1.5 times U_{mf} for two seconds real time. Unfortunately, these simulations are extremely demanding, and only selected simulations were run for a longer duration of fluidization. Preliminary studies showed, that for these simulations the gravity-based Bond scaling must be applied. The results for low Bond numbers ($Bo \leq 0.01$) indicate no influence of cohesion on the minimum fluidization velocity, as well as on the segregation behavior. With increasing Bond number, the minimum fluidization velocity decreases slightly. One reason for this behavior is that, for less cohesive cases, the small particles rearrange in the flow field, indicated by a characteristic decrease of the slope of the pressure drop at $U_0 \approx 1$ mm/s. The pressure drop in the cylindrical setup overshoots at U_{mf} and decreases slowly to the final (reference) value. This behavior cannot be seen for the periodic setup and becomes more pronounced with increasing coarse graining ratio. This leads to the speculation that the overshoot is due to wall effects, following the line of thoughts documented in Jackson [53].

For high Bond numbers, segregation profiles, as well as dumped data, indicate no segregation because the small particles stick to larger ones. For the less cohesive cases, the small particles segregate in clusters through the bed. In the periodic setups, this results in layers of small and larger particles. Thus, simulations with fewer CFD cells in vertical direction, as well as for a longer time were performed to investigate this peculiar arrangement of particles. Results show that for bigger CFD cells these particle clusters become larger and move upwards through the bed. This indicates that the results of our predictions are affected to some extent by grid effects, meaning that one must carefully investigate these effects during calibration.

6.1 Workflow

We propose the following workflow to match experimentally-determined segregation profiles in a lab-scale segregation experiments with simulations:

- *Step 1: Calibration of the particle size distribution*
  Simulation results showed that cohesion has only a weak impact on the minimum fluidization velocity. Thus, in a first step, cohesion can be neglected to calibrate the PSD in the segregation tester setup to reach the required minimum fluidization velocity.
- *Step 2: Calibration of the Hamaker constant*
  Afterwards, calibrate the Hamaker constant of the van der Waals cohesion model in a "two-dimensional symmetric gravity" (e.g. stress until shear) setup to match the yield locus and internal friction angle observed in shear experiments.
- *Step 3: Run the segregation simulations*
  Finally, CFD-DPM simulations must be performed with a proper coarse graining ratio. The scaling of the cohesion model has to be done via the gravity-based Bond number. If necessary, adapt the Hamaker constant and repeat the segregation simulations.

6.2 Outlook

Our simulation results indicate that the scaling of the van der Waals cohesion model depends on the local flow regime in the simulations. Future research could focus on a regime-based scaling of the Hamaker constant considering the following line of thoughts: In dense regimes one could use a linear *CG*-scaling, and in dilute regimes – where the gravitational force is dominating – a quadratic *CG*-scaling could be used.

Recent work of Gu et al. [37] found that decreasing the Young's modulus in cohesive systems yields a wrong flow pattern. Thus, they proposed a modified cohesion model to take this into account. Unfortunately, this thesis was too far advanced when the publication of Gu et al. [37] was accessible. Future work might consider the findings of Gu et al. [37] to compensate the effect of the relatively soft particles used in DEM-based simulations.

7 References

[1] K.J. Berger, C.M. Hrenya, Challenges of DEM: II. Wide particle size distributions, Powder Technol. 264 (2014) 627–633.

[2] A. Rao, J.S. Curtis, B.C. Hancock, C. Wassgren, Classifying the fluidization and segregation behavior of binary mixtures using particle size and density ratios, AIChE J. 57 (2011) 1446–1458.

[3] M. Jaklič, K. Kočevar, S. Srčič, R. Dreu, Particle size-based segregation of pharmaceutical powders in a vertical chute with a closed bottom: An experimental evaluation, Powder Technol. 278 (2015) 171–180.

[4] C. Bierwisch, T. Kraft, H. Riedel, M. Moseler, Die filling optimization using three-dimensional discrete element modeling, Powder Technol. 196.2 (2009) 169–179.

[5] Y. Guo, C.Y. Wu, K.D. Kafui, C. Thornton, Numerical analysis of density-induced segregation during die filling, Powder Technol. 197 (2010) 111–119.

[6] Y. Guo, C.Y. Wu, K.D. Kafui, C. Thornton, 3D DEM/CFD analysis of size-induced segregation during die filling, Powder Technol. 206 (2011) 177–188.

[7] D.B. Hedden, D. Brone, S. Clement, M. McCall, A. Olsofsky, P.J. Patel, et al., Development of an Improved Fluidization Segregation Tester for Use with Pharmaceutical Powders, Pharm. Technol. 30 (2006) 54–64.

[8] J.K. Prescott, S.A. Clement, J.W. Carson, Fluidization segregation tester, U.S. Patent No. 6,487,921, 2002.

[9] M. Wormsbecker, A. Adams, T. Pugsley, C. Winters, Segregation by size difference in a conical fluidized bed of pharmaceutical granulate, Powder Technol. 153 (2005) 72–80.

[10] K. Johanson, Review of new segregation tester method by Dr . Kerry Johanson , P . E ., Powder Technol. 257 (2014) 1–10.

[11] L. Aarons, S. Sundaresan, Shear flow of assemblies of cohesive and non-cohesive granular materials, Powder Technol. 169 (2006) 10–21.

[12] R. Schwarze, A. Gladkyy, F. Uhlig, S. Luding, Rheology of weakly wetted granular materials: a comparison of experimental and numerical data, Granul. Matter. 15 (2013) 455–465.

[13] C.S. Campbell, Granular shear flows at the elastic limit, J. Fluid Mech. 465 (2002) 261–291.

[14] Y. Gu, S. Chialvo, S. Sundaresan, Rheology of cohesive granular materials across multiple dense-flow regimes, Phys. Rev. E. 90 (2014) 032206.

[15] S. Ji, H.H. Shen, Internal parameters and regime map for soft polydispersed granular materials, J. Rheol. 52 (2008) 87–103.

[16] A. Singh, V. Magnanimo, K. Saitoh, S. Luding, Effect of cohesion on shear banding in quasistatic granular materials, Phys. Rev. E. 90 (2014) 022202.

[17] Y. Gu, A. Ozel, S. Sundaresan, Rheology of granular materials with size distributions across dense-flow regimes, Powder Technol. (2016).

[18] R. Beetstra, M.A. van der Hoef, J.A.M. Kuipers, Numerical study of segregation using a new drag force correlation for polydisperse systems derived from lattice-Boltzmann

simulations, Chem. Eng. Sci. 62 (2007) 246–255.

[19] M.J. V Goldschmidt, R. Beetstra, J.A.M. Kuipers, Hydrodynamic modelling of dense gas-fluidised beds: Comparison and validation of 3D discrete particle and continuum models, Powder Technol. 142 (2004) 23–47.

[20] O.O. Olaofe, A. V. Patil, N.G. Deen, M.A. van der Hoef, J.A.M. Kuipers, Simulation of particle mixing and segregation in bidisperse gas fluidized beds, Chem. Eng. Sci. 108 (2014) 258–269.

[21] C. Bierwisch, T. Kraft, H. Riedel, M. Moseler, Three-dimensional discrete element models for the granular statics and dynamics of powders in cavity filling, J. Mech. Phys. Solids. 57 (2009) 10–31.

[22] S. Radl, C. Radeke, J.G. Khinast, S. Sundaresan, Parcel-Based Approach For The Simulation Of Gas-Particle Flows, in: 8th Interantional Conf. CFD Oil Gas, Metall. Process Ind., 2011.

[23] S. Radl, Particle Technology I Lecture Notes, IPPE TU Graz, (2012).

[24] S. Luding, Introduction to discrete element methods: Basic of contact force models and how to perform the micro-macro transition to continuum theory, Eur. J. Environ. Civ. Eng. 12 (2008) 785–826.

[25] C. Kloss, LIGGGHTS(R)-Public Documentation , Version 3.X, (2015).

[26] Y.T. Feng, D.R.J. Owen, Discrete element modelling of large scale particle systems—I: exact scaling laws, Comput. Part. Mech. 1 (2014) 159–168.

[27] R. Beetstra, M.A. van der Hoef, J.A.M. Kuipers, Drag force of intermediate Reynolds number flow past mono- and bidisperse arrays of spheres, AIChE J. 53.2 (2007) 489–501.

[28] W. Holloway, X. Yin, S. Sundaresan, Fluid-particle drag in inertial polydisperse gas–solid suspensions, AIChE J. 56 (2010) 1995–2004.

[29] A.B. Yu, J. Bridgwater, A. Burbidge, On the modelling of the packing of fine particles, Powder Technol. 92 (1997) 185–194.

[30] J.N. Israelachvili, Intermolecular and Surface forces, 2nd ed., Academic: London, 1991.

[31] H.C. Hamaker, The London-van der Waals attraction between spherical particles, Physica. 4 (1937) 1058–1072.

[32] J.P.K. Seville, C.D. Willett, P.C. Knight, Interparticle forces in fluidisation: A review, Powder Technol. 113 (2000) 261–268.

[33] M. Ye, M.A. Van Der Hoef, J.A.M. Kuipers, A numerical study of fluidization behavior of Geldart A particles using a discrete particle model, Powder Technol. 139 (2004) 129–139.

[34] H. Rumpf, Particle Technology, Chapman & Hall, London, 1990.

[35] Y.I. Rabinovich, J.J. Adler, A. Ata, R.K. Singh, B.M. Moudgil, Adhesion between Nanoscale Rough Surfaces, J. Colloid Interface Sci. 232 (2000) 10–16.

[36] Q. Li, V. Rudolph, W. Peukert, London-van der Waals adhesiveness of rough particles, Powder Technol. 161 (2006) 248–255.

[37] Y. Gu, A. Ozel, S. Sundaresan, A modified cohesion model for CFD–DEM simulations of fluidization, Powder Technol. (2015) http://

dx.doi.org/10.1016/j.powtec.2015.09.037.

[38] K.L. Johnson, K. Kendall, A.D. Roberts, Surface energy and the contact of elastic solids, Proc. R. Soc. London A Math. Phys. Eng. Sci. 324 (1971) 301–313.

[39] B. V Derjaguin, V.M. Muller, Y.U.P. Toporov, Effect of contact deformation on the adhesion of particles., J. Colloid Interface Sci. 53 (1975) 314–326.

[40] D.S. Nasato, C. Goniva, S. Pirker, C. Kloss, Coarse Graining for Large-Scale DEM Simulations of Particle Flow – An Investigation on Contact and Cohesion Models, Procedia Eng. 102 (2015) 1484–1490.

[41] Z. Yan, S.K. Wilkinson, S. a Turnbull, E.H. Stitt, M. Marigo, Parametric evaluation for powder flowability using a freeman rheometer: a discrete element method study, in: PARTICLES, 2015: pp. 854–865.

[42] J.E. Galvin, S. Benyahia, The effect of cohesive forces on the fluidization of aeratable powders, AIChE J. 60 (2014) 473–484.

[43] R.Y. Yang, R.P. Zou, A.B. Yu, Computer simulation of the packing of fine particles, Phys. Rev. E. 62 (2000) 3900–3908.

[44] O.R. Walton, Potential discrete element simulation applications ranging from airborne fines to pellet beds, SAE 2004 Trans. J. Aerosp. (2004).

[45] J. Schwedes, Review on testers for measuring flow properties of bulk solids, Granul. Matter. 5 (2003) 1–43.

[46] A.W. Jenike, Storage and Flow of Solids, Bulletin 123, Engineeging Experiment Station, University of Utah, (1964).

[47] R. Beckhaus, W. Felgner, J. Runge, Auslegung von Silos für verklebende grobkörnige Schüttgüter, Chemie Ing. Tech. 64 (1992) 292–293.

[48] S. Luding, F. Alonso-Marroquín, The critical-state yield stress (termination locus) of adhesive powders from a single numerical experiment, Granul. Matter. 13 (2011) 109–119.

[49] A.W. Lees, S.F. Edwards, The computer study of transport processes under extreme conditions, J. Phys. C Solid State Phys. 5 (1972) 1921–1929.

[50] M. Stieß, Mechanische Verfahrenstechnik - Partikeltechnologie 1, Springer-Verlag, 2009.

[51] B.C. González, Advanced Drag Models for Bi-Disperse Bubbling Fluidized Beds, Graz University of Technology, 2013.

[52] N.N., [Online]. Available: http://www.engineeringtoolbox.com/air-properties-d_156.html. [Accessed: 01-Jun-2015], (n.d.).

[53] R. Jackson, The dynamics of fluidized particles, Cambridge University Press, 2000.

[54] F. Holzinger, Modification of Filtered Drag Models for Polydisperse Flows, Graz University of Technology, 2015.

[55] M. Boton, E. Azéma, N. Estrada, F. Radjaï, A. Lizcano, Quasistatic rheology and microstructural description of sheared granular materials composed of platy particles, Phys. Rev. E. 87 (2013) 032206.

[56] S. Chialvo, J. Sun, S. Sundaresan, Bridging the rheology of granular flows in three regimes, Phys. Rev. E. 85.2 (2012) 021305.

[57] Z.Y. Zhou, S.B. Kuang, K.W. Chu, A.B. Yu, Discrete particle simulation of particle–

fluid flow: model formulations and their applicability, J. Fluid Mech. 661 (2010) 482–510.

Appendix A - Simulation Details

A.1 Fluid-Particle Interactions

In this work the fluid-particle interactions on each particle are modeled with the following forces:

- the pressure gradient force $\mathbf{F}_{\nabla P}$,
- the viscous force $\mathbf{F}_{\nabla\cdot\boldsymbol{\tau}}$, and
- the drag force $\mathbf{F}_d$.

While the pressure gradient force and the viscous force remained unchanged all Euler-Lagrange simulations in this study, two different definition of the drag force are used: (i) the Beetstra monodisperse drag model [27], and (ii) the Holloway drag model [28] for polydisperse flows.

The “gradPForce” model in CFDEM® calculates the pressure gradient force, acting on a particle as [57]:

$$\mathbf{F}_{\nabla P} = -\nabla p \cdot V_p \tag{A.1}$$

The “viscForce” model in CFDEM® calculates the particle based viscous force due to the fluid shear or deviatoric stress tensor as [57]:

$$\mathbf{F}_{\nabla\cdot\boldsymbol{\tau}} = -\left(\nabla \cdot \boldsymbol{\tau}\right) V_p \tag{A.2}$$

Here V_p is the particle volume.

A.1.1 The Beetstra Monodisperse Drag Model

Beetstra et al. [27] proposed a drag force model for dense particulate systems, based on lattice-Boltzmann simulations of arrays of monodisperse spheres. They use the Stokes drag force to scale the drag force and define a dimensionless drag force $F\left(\phi_p, Re\right)$ as:

$$F\left(\phi_p, Re\right) = \frac{\mathbf{F}_d}{3\pi\,\mu_f\, d_p\left(\mathbf{u}_f - \mathbf{u}_p\right)} \tag{A.3}$$

$$F\left(\phi_p, Re\right) = \frac{10\phi_p}{\left(1-\phi_p\right)^2} + \left(1-\phi_p\right)^2\left(1+1.5\phi_p^{1/2}\right) + \frac{0.413\,Re}{24\left(1-\phi_p\right)^2}\left[\frac{\left(1-\phi_p\right)^{-1} + 3\phi_p\left(1-\phi_p\right) + 8.4\,Re^{-0.343}}{1+10^{3\phi_p}\,Re^{-\left(1+4\phi_p\right)/2}}\right] \tag{A.4}$$

Here the Reynolds number is defined with the superficial velocity between the fluid and the particle:

$$Re = \frac{d_p\left|\mathbf{u}_f - \mathbf{u}_p\right|\phi_f}{\nu_f} \tag{A.5}$$

A.1.2 The Holloway Drag Model

Beetstra et al. [27] also proposed a modified drag force model for bidisperse systems, which takes the presence of other particle species into account. Holloway et al. [28] extended this model to apply to polydisperse suspensions with high Stokes numbers and moderate Reynolds numbers. This, so-called, advanced drag model requires additional information about the system: (i) the local Sauter mean diameter, (ii) the mixture Reynolds number, and (iii) individual particle species information. Moreover, this force model also accounts for the fluid-mediated particle-particle drag in polydisperse systems. Detailed information about the Holloway drag model can be found elsewhere [28,51].

The force sub model “ImExCorr” in CFDEM® is an extension of the “ImEx” model that additionally corrects the error stemming from the interpolation of the fluid and particle velocities. In this work the “ImExCorr” model is only activated for the Holloway drag model [28], and one time with the Beetstra drag model [27].

A.2 The Stress Tensor

The macroscopic stress tensor $\boldsymbol{\sigma}$ is the sum of contact stress due to particle collisions $\boldsymbol{\sigma}_{cont}$, and the kinetic stress due to velocity fluctuations of the particles $\boldsymbol{\sigma}_{kin}$ [23]:

$$\boldsymbol{\sigma} = \frac{1}{\Delta V_i}\sum_{p\in\Delta V_i} w_{p,\Delta V}\left(\sum_{c=1}^{c^p}\mathbf{F}^c \otimes \mathbf{l}^{pc} + m_p\mathbf{u}'_p \otimes \mathbf{u}'_p\right) \tag{A.6}$$

The principal diagonal elements are the normal stresses σ_{ii}, and the others are called shear stresses τ_{ij}:

$$\boldsymbol{\sigma} = \begin{bmatrix} \sigma_{xx} & \tau_{xy} & \tau_{xz} \\ \tau_{yx} & \sigma_{yy} & \tau_{yz} \\ \tau_{zx} & \tau_{zy} & \sigma_{zz} \end{bmatrix} \tag{A.7}$$

The shear stresses are symmetric with respect to the principal diagonal:

$$\tau_{xy} = \tau_{yx} \qquad \tau_{xz} = \tau_{zx} \qquad \tau_{yz} = \tau_{zy} \tag{A.8}$$

The pressure (or hydrostatic stress) of a granular material is the average of the three normal stress components:

$$\sigma = \frac{\sigma_{xx} + \sigma_{yy} + \sigma_{zz}}{3} \tag{A.9}$$

Appendix B - Simulation Setups

Appendix B is only available in the electronic version. This appendix consists of the following directories and files:

octave

Octave functions that have been used in the present work

segregationTester

Work directory for segregation tester simulations in the cylindrical domain

segregationTesterPeriodic

Work directory for segregation tester simulations in the periodic domain

shearFlowLE

Work directory for shear flow simulations with Lees-Edwards boundary conditions

stressUntilShear

Work directory for stress until shear simulations